



Published in final edited form as:

Cancer Discov. 2019 February ; 9(2): 282–301. doi:10.1158/2159-8290.CD-18-0710.

IL-1-induced JAK/STAT signaling is antagonized by TGF- β to shape CAF heterogeneity in pancreatic ductal adenocarcinoma.

Giulia Biffi¹, Tobiloba E. Oni¹, Benjamin Spielman¹, Yuan Hao¹, Ela Elyada¹, Youngkyu Park¹, Jonathan Preall¹, and David A. Tuveson^{1,*}

¹Cold Spring Harbor Laboratory, Cold Spring Harbor, NY 11724

Abstract

Pancreatic ductal adenocarcinoma (PDAC) is poorly responsive to therapies and histologically contains a paucity of neoplastic cells embedded within a dense desmoplastic stroma. Within the stroma, cancer-associated fibroblasts (CAFs) secrete tropic factors and extracellular matrix components, and have been implicated in PDAC progression and chemotherapy resistance. We recently identified two distinct CAF subtypes characterized by either myofibroblastic or inflammatory phenotypes; however, the mechanisms underlying their diversity and their roles in PDAC remain unknown. Here, we use organoid and mouse models to identify TGF- β and IL-1 as tumor-secreted ligands that promote CAF heterogeneity. We show that IL-1 induces LIF expression and downstream JAK/STAT activation to generate inflammatory CAFs, and demonstrate that TGF- β antagonizes this process by downregulating IL-1R1 expression and promoting differentiation into myofibroblasts. Our results provide a mechanism through which distinct fibroblast niches are established in the PDAC microenvironment and illuminate strategies to selectively target CAFs that support tumor growth.

Keywords

Pancreatic cancer; CAF heterogeneity; JAK/STAT signaling; IL-1; TGF- β

INTRODUCTION

With an overall 5-year survival of less than 8%, pancreatic ductal adenocarcinoma (PDAC) is one of the cancers with the worst prognosis (1). Among the reasons for PDAC lethality, late diagnosis and resistance to chemotherapy play a central role. Factors that contribute to this resistance include the presence of a poorly vascularized, extensive stroma that acts as a barrier to drug delivery (2-5), and cytokines and growth factors secreted by non-neoplastic stromal cells that attenuate drug responses (6-10). While numerous studies have focused on the genetic and epigenetic forces that drive PDAC progression, less is understood about the complex tumor microenvironment (TME).

*Corresponding author: David A. Tuveson, Cold Spring Harbor laboratory, 1 Bungtown road, Cold Spring Harbor, New York, NY 11724. Phone: 516-367-5246; Fax: 516-367-8353; dtuveson@cshl.edu.

Disclosure of potential conflict of interest: The authors declare no potential conflicts of interest.

Previous studies that targeted different stromal cell types or extracellular matrix components, such as hyaluronan, have highlighted the presence of both tumor-promoting and tumor-restraining components in the PDAC stroma. Among stromal cells, cancer-associated fibroblasts (CAFs) have long been considered pro-tumorigenic components of the PDAC TME, due to their involvement in desmoplasia, immunosuppression and secretion of factors that promote cancer cell proliferation and survival (2,4,11,12). However, in recent years, CAFs have been the focus of an active debate that has challenged this dogma. In mouse models of PDAC, targeting of the hedgehog (HH) pathway, which has been shown to stimulate CAF biology, by genetic deletion of the ligand sonic hedgehog (SHH) or chronic chemical inhibition, led to more aggressive and poorly differentiated PDAC, with reduced stromal content and accelerated disease (13,14). Furthermore, a clinical trial employing inhibition of the HH pathway failed in advanced PDAC (15). These results suggest that at least a subset of CAFs plays a role in restricting, rather than promoting, tumor progression. Moreover, genetic ablation of cells expressing smooth muscle actin (α SMA), a marker of myofibroblasts, led to similar results in a mouse model of PDAC (16), suggesting that perturbation of myofibroblastic components in the PDAC TME might promote tumor progression. Overall, these studies highlight the heterogeneity of PDAC stroma, prompting a more detailed examination of the role of the TME in PDAC progression, and calling for new therapeutic strategies that selectively target tumor-promoting CAF populations and spare tumor-restraining ones.

To better understand tumor-fibroblast interactions in PDAC, we recently established a system to co-culture naïve pancreatic stellate cells (PSCs), a precursor population of CAFs, with PDAC organoids derived from KPC (*Kras*^{LSL-G12D/+}; *Tip53*^{LSL-R172H/+}; *Pdx1-Cre*) mice, a genetically engineered mouse model that faithfully recapitulates human PDAC progression (17-19). Using this system, as well as *in vivo* mouse and human PDAC specimens, we identified two subtypes of CAFs: a population that expressed inflammatory markers such as interleukin 6 (IL-6) and leukemia inhibitory factor (LIF) and was therefore named “inflammatory CAFs” (iCAFs), and a population that expressed markers of myofibroblasts, such as α SMA, and was therefore named “myofibroblastic CAFs” (myCAFs) (19). While myCAFs are found adjacent to tumor cells, iCAFs are located farther away within the dense stroma, suggesting that their different phenotypes might be related to their spatial distribution. Importantly, the presence of iCAF and myCAF populations in human PDAC *in vivo* has been recently confirmed (20). However, the signals that drive the formation of these distinct populations are not known. To better understand the mechanisms that promote the formation of these two CAF populations in PDAC, we focused on the identification of tumor-secreted ligands and signaling pathways responsible for their respective phenotypes.

RESULTS

Active NF- κ B signaling is associated with the iCAF phenotype

We first sought to define signaling pathways that are upregulated in iCAFs compared to myCAFs and quiescent PSCs. Since many of the factors secreted by iCAFs, such as IL-6, granulocyte-colony stimulating factor (G-CSF), chemokine (C-X-C motif) ligand 1

(CXCL1) and LIF have been shown to play a role in tumor progression (21-24), targeting this CAF population might be therapeutically beneficial. We hypothesized that NF- κ B signaling might play a role in iCAF formation, as it has been previously identified as a pathway responsible for the induction of an inflammatory profile in CAFs (25,26).

The role of the NF- κ B pathway and of its activating ligands interleukin-1 (IL-1) and tumor-necrosis factor alpha (TNF- α) in PDAC progression have been mostly studied in the context of the epithelial compartment (27-31). However, some studies have reported a role of tumor-secreted IL-1 and TNF- α in remodeling PDAC stroma (32-34). In particular, IL-1 α has been shown to induce the expression of IL-6 and chemokine (C-X-C motif) ligand 8 (CXCL8), in PDAC CAFs *in vitro* (32). To determine whether IL-1 and TNF- α signaling can be activated in PDAC CAFs *in vivo*, we sorted neoplastic epithelial cells and CAFs from tumors isolated from KPC mice. Epithelial cell adhesion molecule (EpCAM) and platelet-derived growth factor receptor alpha ((PDGFR α)/podoplanin (PDPN) expression were used to sort epithelial cells and CAFs, respectively (Supplementary Figure S1A). qPCR analysis on the sorted populations showed that *Il1a* and *Tnf* were more highly expressed in epithelial cancer cells relative to CAFs, whereas the corresponding receptors that trigger NF- κ B activation (*Il1r1* and *Tnfrsf1a*) were predominantly expressed in CAFs (Figure 1A). Consistent with this observation, flow cytometric analysis of CAFs and epithelial cells isolated from KPC tumors identified higher levels of IL-1R1 protein in CAFs compared to epithelial cancer cells (Figure 1B; Supplementary Figure S1B). As a complementary approach, single cell RNA-sequencing analysis of KPC tumors confirmed higher expression of the ligands activating the NF- κ B pathway in epithelial cells and higher expression of their receptors in CAFs (Figure 1C; Supplementary Figure S1C). Altogether, these results demonstrate that CAFs are poised to respond to the ligands that activate the NF- κ B pathway.

While IL-1 β was not detectable *in vitro* (data not shown), IL-1 α and TNF- α were detectable by enzyme-linked immunosorbent assay (ELISA) in conditioned media from tumor and metastatic organoids as well as monolayer KPC cell lines, but not in conditioned media from fibroblasts. This agrees with the observation that fibroblasts are not capable to stimulate iCAF formation (19) (Figure 1D; Supplementary Figure S1D).

To model iCAF, myCAF and quiescent fibroblast states, we employed distinct culture conditions (19). PSCs embedded in Matrigel and cultured in control media (5% FBS/DMEM) maintain a quiescent phenotype. In contrast, PSCs embedded in Matrigel and cultured in a transwell system with tumor organoids or exposed to tumor organoid-conditioned media acquire an inflammatory phenotype characteristic of iCAFs. Finally, PSCs cultured in monolayer acquire the myofibroblastic features characteristic of myCAFs (Supplementary Figure S1E).

To verify that the *in vitro* culture systems used to model iCAFs and myCAFs closely resemble the *in vivo* setting, we analyzed the single cell RNA-sequencing dataset of KPC tumors. Confirming our previous findings (19), single cell RNA-sequencing analysis of KPC tumors revealed *in vivo* presence of both iCAF and myCAF populations (Supplementary Figure S1F). Similar to what observed *in vitro* (19), the iCAFs and myCAFs identified *in vivo* segregated in two distinct clusters (Supplementary Figure S1G). We then compared the

gene expression profiles of myCAFs and iCAFs identified *in vivo* to the gene expression profiles of myCAFs and iCAFs cultured *in vitro*, as previously reported by our laboratory (19). Venn diagrams of genes upregulated in iCAFs or myCAFs showed significant overlap between the *in vivo* and *in vitro* datasets (Supplementary Figure S1H), supporting the *in vivo* relevance of our *in vitro* system. To further support this, gene set enrichment analysis of iCAFs and myCAFs identified *in vivo* revealed several differentially expressed pathways that were previously identified by our laboratory using the *in vitro* system (19). For instance, JAK/STAT pathway was upregulated in iCAFs compared to myCAFs, while collagen formation and transforming growth factor beta (TGF- β) signaling pathways were downregulated in iCAFs compared to myCAFs (Supplementary Figure S1I).

Having established the reliability of our *in vitro* system, we first investigated whether the NF- κ B pathway has a role in iCAF formation. Using the *in vitro* culture conditions described (Supplementary Figure S1E), we prepared nuclear protein extracts from quiescent PSCs, iCAFs and myCAFs, and evaluated activation of the NF- κ B pathway. Fractionation experiments revealed that nuclear levels of the NF- κ B p65 subunit were more elevated in iCAFs compared to quiescent PSCs and myCAFs (Figure 1E). Moreover, activation of p65 occurred rapidly in PSCs cultured in Matrigel upon addition of tumor organoid-conditioned media, as shown by increased levels of phosphorylated p65, parallel to phosphorylation of the NF- κ B inhibitor I κ B α (p-I κ B α), which is followed by its rapid degradation (Supplementary Figure S1J), suggesting a role of the NF- κ B pathway in iCAF formation. Treatment with ML102B, which targets inhibitor of nuclear factor kappa-B kinase subunit beta (IKK- β) (35), impaired activation of the pathway, as shown by inhibition of p65 phosphorylation and stabilization of total I κ B α (Figure 1F). To confirm that NF- κ B promotes iCAF formation, we thus determined the effects of NF- κ B pathway inhibition on the expression of iCAF markers, such as *Il1a*, *Il6*, *Lif*, *Cxcl1* and *Csf3* (encoding for G-CSF). Inhibition of NF- κ B signaling impaired the ability of tumor organoid-conditioned media to induce iCAF marker genes in PSCs, supporting the premise that NF- κ B signaling is required for the formation of iCAFs (Figure 1G).

IL-1 signaling is the main pathway responsible for the induction of an inflammatory phenotype in CAFs

To evaluate whether ligands that activate the NF- κ B pathway induce the iCAF phenotype in quiescent PSCs, we cultured mouse and human PSCs in Matrigel in the presence or absence of IL-1 α . In response to IL-1 α , both mouse and human PSCs increased expression of multiple inflammatory cytokines and chemokines, such as *Il1a*, *Il6*, *Lif*, *Cxcl1* and *Csf3* (Figure 2A; Supplementary Figure 2A and 2B). In parallel, IL-1 α treatment led to a decreased expression of myofibroblastic genes, such as the TGF- β target gene connective tissue growth factor (*Ctgf*) and the α SMA gene *Acta2*, suggesting that IL-1 α promotes the iCAF phenotype (19) (Figure 2A; Supplementary Figure 2A and 2B). Similar to IL-1 α , IL-1 β and TNF- α were also sufficient to induce iCAF marker genes and downregulate myofibroblastic genes in PSCs (Supplementary Figure S2C).

Having established that IL-1 α and TNF- α are both secreted by cancer cells and sufficient to induce iCAF markers, we determined whether these NF- κ B signaling activators are

necessary for the induction of the iCAF phenotype. Neutralization of TNF- α did not impair the induction of iCAF markers in PSCs cultured with tumor organoid-conditioned media (Supplementary Figure S2D). However, targeting IL-1 α with a neutralizing antibody significantly reduced induction of iCAF marker genes and partially restored expression of myofibroblastic genes in PSCs exposed to tumor organoid-conditioned media (Figure 2B). In addition, IL-1 α neutralization significantly impaired the proliferation of PSCs cultured as iCAFs, but not of PSCs cultured as myCAFs, suggesting that IL-1 α plays a key role in the iCAF phenotype (Figure 2C; Supplementary Figure S2E).

To confirm the role of tumor-secreted IL-1 α in establishing the iCAF phenotype, we employed CRISPR/Cas9 to knock out IL-1 α in tumor organoids (Supplementary Figure S2F). We co-cultured these organoids with PSCs in transwells to model iCAFs, as previously described (19) (Supplementary Figure S1E). Levels of the iCAF markers were significantly reduced when PSCs were cultured with IL-1 α knockout organoids compared to Rosa26-targeted control organoids, while levels of the myCAF marker α SMA were significantly increased (Figure 2D). As an orthogonal approach, to confirm that IL-1 signaling is the major pathway responsible for iCAF formation *in vitro*, we knocked out IL-1 receptor (IL-1R1) in PSCs (Supplementary Figure S2G). As expected, when PSCs were cultured in transwells with tumor organoids, levels of the iCAF markers were lower in IL-1R1 knockout compared to Rosa26-targeted control PSCs, while myofibroblastic genes were higher (Figure 2E). To confirm that the impaired acquisition of the iCAF phenotype was a direct consequence of IL-1R1 deletion, we ectopically expressed guide-resistant IL-1R1 constructs in three knockout clones (Supplementary Figure S2H). Expression of IL-1R1 rescued the iCAF phenotype when PSCs were cultured with tumor organoid-conditioned media, confirming that IL-1R1 is essential for the induction of iCAF markers (Supplementary Figure S2I). Finally, we isolated 2 primary PSC lines from IL-1R1 knockout mice (36) (Supplementary Figure S2J) and cultured them in the presence of IL-1 α . Contrary to what we observed in primary IL-1R1 wild-type PSCs (Supplementary Figure S2A), IL-1 α treatment did not promote the iCAF phenotype in primary IL-1R1-deficient PSCs (Supplementary Figure S2K). Altogether, these results support a key role of IL-1 signaling in inducing the iCAF phenotype *in vitro*.

To investigate the role of IL-1 α in inducing the iCAF phenotype *in vivo*, we orthotopically transplanted Rosa26-targeted controls and three lines of IL-1 α -deficient tumor organoids in nu/nu mice to generate orthotopically grafted organoids (OGOs) (17). These three IL-1 α knockout lines showed different proliferative properties *in vitro* (Figure 2F). Notably, all three lines of IL-1 α -deficient organoids formed significantly smaller tumors compared to control organoids (Figure 2G). Collagen deposition and α SMA levels did not significantly differ between control OGOs and IL-1 α knockout OGOs (Supplementary Figure S3A, S3B, S3C and S3D), suggesting there is no increase in myofibroblastic CAFs *in vivo* in the absence of tumor-secreted IL-1 α . We then investigated whether the growth defect of IL-1 α knockout tumors is associated with a reduced presence of iCAFs in the PDAC microenvironment. We, thus, sorted CAFs from the tumors derived by transplants of the IL-1 α knockout organoid lines or Rosa26-targeted controls using EpCAM and PDGFR α /PDPN markers (Supplementary Figure S1A). We then assessed the transcript level of inflammatory and myofibroblastic genes and observed a consistent reduction in *Il1a* and

Csf3 in CAFs of tumors derived from the knockout lines compared to the controls (Figure 2H). The decrease in G-CSF levels may be responsible for the reduced tumor growth observed *in vivo*, since G-CSF has been shown to be involved in PDAC progression (37,38). However, this analysis showed only a partial response towards a less inflammatory CAF phenotype, suggesting that IL-1 α is not the only ligand that can induce iCAF formation *in vivo*. This agrees with the observation that IL-1 β and TNF- α are also sufficient to induce an iCAF phenotype *in vitro* (Supplementary Figure S2C) and have been shown to play a role in PDAC fibrosis (33,34). In order to address the role of IL-1 β and TNF- α *in vivo*, we sorted EpCAM⁺ cells from OGOs of IL-1 α knockout organoids or Rosa26-targeted controls and assessed *Il1b* and *Tnf* transcript levels. While *Il1b* transcript is undetectable in tumor organoids *in vitro*, it is expressed *in vivo* in the epithelial compartment of both controls and IL-1 α knockout tumors (Supplementary Figure S3E). Similarly, *Tnf* transcript was more elevated in epithelial cells of both controls and IL-1 α knockout tumors compared to organoids *in vitro* (Supplementary Figure S3F). Altogether, these results demonstrate that deletion of tumor-derived IL-1 α impairs tumorigenesis and CAF expression of IL-1 α and G-CSF, but is not sufficient to fully prevent induction of an inflammatory stroma *in vivo*.

To circumvent the redundancy of IL-1 isoforms and assess the role of IL-1 signaling in inducing the iCAF phenotype *in vivo*, we orthotopically transplanted three tumor organoid lines in either IL-1R1 knockout mice (36) or C57BL/6J controls. Quantification of collagen deposition and α SMA levels revealed a trend towards an increase of these parameters in tumors developed in IL-1R1-deficient hosts (Supplementary Figure S3G, S3H, S3I and S3J). In order to assess whether iCAF formation is impaired in the absence of IL-1 signaling *in vivo*, we sorted CAFs from the OGOs using EpCAM and PDGFR α /PDPN markers (Supplementary Figure S1A) and measured the transcript levels of inflammatory and myofibroblastic genes. iCAF markers were downregulated in CAFs sorted from tumors grown in IL-1R1 knockout hosts compared to tumors grown in IL-1R1 wild-type hosts, parallel to a modest, yet significant increase in myCAF marker gene expression (Figure 2I).

We then used our flow cytometry strategy (Supplementary Figure S1B) combined with flow cytometric analysis of LY6C, a surface marker that distinguishes a subset of iCAFs (Supplementary Figure S1G, S3K and S3L) to analyze myCAF and iCAF populations in tumors grown in IL-1R1 knockout or wild-type hosts. In agreement with the analysis of transcript levels of inflammatory and myofibroblastic markers in CAFs (Figure 2I), the results showed a decrease in Ly6C⁺ iCAFs in tumors grown in IL-1R1 knockout hosts compared to tumors grown in IL-1R1 wild-type hosts (Figure 2J; Supplementary Figure S3M and S3N). Altogether, these results confirm a major role of tumor-secreted IL-1 and stromal IL-1R1 signaling in the formation of iCAFs *in vivo*.

IL-1-mediated induction of autocrine LIF in PSCs activates JAK/STAT signaling and promotes iCAF formation

To examine the downstream pathways activated by IL-1 signaling that contribute to iCAF formation, we assessed the acute expression of inflammatory cytokines and chemokines, which are potential signaling effectors, in response to IL-1 α . Following exposure of PSCs to IL-1 α for one hour, iCAF marker genes were upregulated, suggesting that IL-1 signaling

directly regulates the expression of these genes (Figure 3A). A number of iCAF markers that are quickly induced by IL-1 α (e.g. IL-6, G-CSF and LIF) are known activators of the JAK/STAT signaling pathway (19,21-23). In addition, the JAK/STAT transcriptional signature was previously found to be significantly upregulated in iCAFs compared to quiescent PSCs *in vitro* (19) and in iCAFs compared to myCAFs *in vivo* (Supplementary Figure S11). Accordingly, JAK/STAT pathway members JAK1, JAK2, STAT3 and STAT1 were more highly activated in iCAFs compared to myCAFs and quiescent PSCs (Supplementary Figure S4A). We therefore hypothesized that JAK/STAT signaling is involved in iCAF formation. We first assessed activation of the JAK/STAT pathway in response to IL-1 α and observed that treatment of quiescent PSCs with IL-1 α induces activation of JAK/STAT signaling (Figure 3B). Moreover, neutralization of IL-1 α with an antibody significantly inhibited the JAK/STAT pathway in PSCs cultured with tumor organoid-conditioned media (Figure 3C). Together, these results suggest that IL-1 α is both necessary and sufficient for JAK/STAT signaling activation in iCAFs. Accordingly, while conditioned media from Rosa26-targeted tumor organoids activated JAK/STAT signaling in PSCs as expected, conditioned media from IL-1 α knockout organoids was unable to activate the pathway (Figure 3D).

To determine which activators of the JAK/STAT pathway promote the iCAF phenotype in an autocrine manner, we exposed PSCs to tumor organoid-conditioned media in which LIF, IL-6 or G-CSF had been neutralized by antibodies, and assayed for activation of iCAF marker genes. Neutralization of LIF led to significant downregulation of the iCAF markers *Il1a*, *Il6* and *Csf3*, with partial restoration of the myofibroblastic markers (Figure 3E). Accordingly, treatment with a LIF-neutralizing antibody blocked activation of the JAK/STAT pathway (Figure 3F), confirming that LIF has a major role in the activation of JAK/STAT signaling in iCAFs. In contrast, neutralization of G-CSF or IL-6 did not reduce the expression of iCAF marker genes nor increase myCAF gene levels (Supplementary Figure S4B and S4C), suggesting that these ligands are not major mediators of the iCAF phenotype. Accordingly, tumor organoid-conditioned media activated JAK/STAT signaling in IL-6 knockout PSCs at levels comparable to PSC controls (Supplementary Figure S4D). Together, our results support a model in which autocrine PSC-derived LIF induced downstream of IL-1 signaling activates JAK/STAT signaling and promotes the iCAF phenotype in PSCs. In support of this model, LIF could be detected in conditioned media from PSCs treated with IL-1 α (Supplementary Figure S4E). To further confirm the role of autocrine LIF from PSCs in mediating induction of iCAF marker genes, we knocked out LIF in PSCs (Supplementary Figure S4F). LIF deletion significantly impaired induction of iCAF marker genes in PSCs cultured in transwell with tumor organoids compared to Rosa26-targeted control PSCs (Figure 3G). In addition, LIF deletion reduced JAK/STAT activation in PSCs exposed to tumor organoid-conditioned media (Supplementary Figure S4G). Altogether, these results implicate autocrine LIF from PSCs as the major mediator of the inflammatory phenotype and JAK/STAT activation in iCAFs.

JAK/STAT signaling mediates the induction of the iCAF phenotype

Having established that tumor-derived IL-1 α induces JAK/STAT signaling through upregulation of LIF, and that LIF is involved in the induction of iCAF markers, we next wanted to determine whether JAK/STAT signaling *per se* is necessary for iCAF formation.

To that end, we cultured PSCs with either IL-1 α or tumor organoid-conditioned media in the presence or absence of the JAK inhibitor AZD1480 (39). As expected, JAK inhibition prevented activation of JAK/STAT signaling in response to IL-1 α or tumor organoid-conditioned media (Supplementary Figure S5A and S5B). In addition, JAK inhibition significantly reduced the upregulation of iCAF markers and the downregulation of myCAF markers that occur in response to tumor organoid-conditioned media or IL-1 α (Figure 4A; Supplementary Figure S5A-S5D). Moreover, inhibition of JAK/STAT signaling led to profound impairment of the proliferation of PSCs cultured as iCAFs (Figure 4B), while only modestly affecting the proliferation of PSCs cultured as myCAFs (Supplementary Figure S5E). These results support a dominant role of JAK/STAT signaling in iCAF formation, and are in line with the observation that JAK/STAT signaling is more active in iCAFs compared to myofibroblasts (Supplementary Figure S4A). In addition, comparison of the expression profiles of quiescent PSCs and PSCs cultured as iCAFs in the presence or absence of the JAK inhibitor revealed that JAK inhibition *in vitro* maintains PSCs in a quiescent cell state (Figure 4C; Supplementary Table S1). As expected, JAK/STAT and cytokine signaling pathways were downregulated following treatment with the JAK inhibitor by gene set enrichment analysis, whereas pathways characteristic of myofibroblasts, such as smooth muscle contraction and collagen formation were significantly upregulated (Supplementary Figure S5F). Impairment of the iCAF signature by inhibition of JAK/STAT signaling was not a consequence of a quiescent, non-proliferative state, as a 24-hour treatment with the JAK inhibitor was sufficient to block the expression of inflammatory genes and restore *Acta2* and *Ctgf* levels in established iCAFs (Figure 4D; Supplementary Figure S5G), without impairing their proliferation (Supplementary Figure S5H). Altogether, these results indicate that, downstream of IL-1 signaling, the JAK/STAT pathway is actively responsible for the iCAF phenotype.

In order to investigate which transcription factors in the JAK/STAT pathway promote iCAF formation, we independently deleted either STAT1 or STAT3 in PSCs. STAT1 knockout did not significantly affect the expression of iCAF marker genes in PSCs cultured in transwell with tumor organoids compared to Rosa26-targeted controls (Supplementary Figure S5I and S5J). In contrast, STAT3 knockout PSCs showed significantly reduced expression of iCAF marker genes with increased *Ctgf* levels when cultured in transwell with tumor organoids (Figure 4E; Supplementary Figure S5K). To corroborate a role for STAT3 in regulating iCAF marker genes, we performed DNA motif analysis on the promoters of genes differentially expressed between myofibroblasts and iCAFs in our previous RNA-sequencing dataset (19). Indeed, STAT3 motifs were enriched in the promoters of a number of iCAF genes, including the promoters of *Il6* and *Csf3* ($p < 0.001$; Supplementary Table S1). Moreover, analysis of ENCODE human STAT3 chromatin immunoprecipitation coupled with high-throughput deep sequencing (ChIP-seq) datasets (UCSC browser) confirmed STAT3 binding at these promoters (40).

STAT3 motifs were also identified in the promoters of both mouse and human *IL1R1* gene ($p < 0.001$; Supplementary Table S1), and ENCODE human STAT3 ChIP-seq datasets (UCSC browser) revealed STAT3 binding at the *IL1R1* promoter (40). Accordingly, IL-1R1 expression was significantly upregulated in iCAFs compared to myCAFs (Figure 4F; Supplementary Figure S5L), whereas it was significantly downregulated in PSCs where

STAT3 was knocked out or in PSCs cultured with tumor organoid-conditioned media in the presence of the JAK inhibitor (Figure 4G; Supplementary Figure S5M and S5N). These results support the presence of a positive feedback loop whereby the iCAF phenotype is maintained through IL-1-dependent activation of JAK/STAT signaling, which in turn leads to the upregulation of IL-1R1 expression.

Our data indicate that JAK/STAT signaling promotes an iCAF phenotype *in vitro*. To determine whether JAK/STAT signaling is active in iCAFs *in vivo*, we performed immunofluorescence co-staining of phosphorylated STAT3 (p-STAT3) and α SMA in KPC tumors and human PDAC. Levels of p-STAT3 were found to be low in α SMA-positive myCAFs surrounding the tumor cells (Figure 4H; Supplementary Figure S5O, arrows). Whereas a small number of α SMA-positive, p-STAT3-positive myofibroblasts could be detected (Figure 4H, Supplementary Figure S5O, asterisk), multiple α SMA-negative, p-STAT3-positive cells were located in the stroma farther away from tumor cells (Figure 4H; Supplementary Figure S5O, arrowheads). This analysis showed significantly higher number of p-STAT3-negative myofibroblasts compared to p-STAT3-positive α SMA-positive cells (Figure 4I; Supplementary Figure S5P), demonstrating that JAK/STAT signaling is low in myCAFs in mouse and human PDAC.

TGF- β signaling antagonizes IL-1-induced JAK/STAT signaling and inhibits the iCAF phenotype

While we have shown that iCAF formation is dependent upon tumor-secreted IL-1 that activates a LIF/JAK/STAT-dependent cytokine cascade, the mechanisms underlying myCAF biology remain unknown. We hypothesized that myCAF formation could be dependent on juxtacrine signals or paracrine signals that are produced by adjacent tumor cells. Previous expression analysis identified enrichment of TGF- β target genes in the myCAF signature compared to quiescent PSCs and iCAFs (19). Given that TGF- β is known to promote a myofibroblast phenotype (41,42), we investigated whether TGF- β signaling could be a dominant feature in this CAF subtype.

To measure TGF- β signaling in the various CAF populations, we prepared cellular and nuclear protein extracts from PSCs cultured as quiescent PSCs, iCAFs or myCAFs, and evaluated activation of the TGF- β pathway. As expected, PSCs cultured as myCAFs had increased expression of the myofibroblastic marker α SMA (Figure 5A). In addition, whereas the levels of total SMAD2 and SMAD3, two effectors of TGF- β signaling, were comparable in different PSC states, myCAFs had elevated levels of phosphorylated SMAD2 and SMAD3 (p-SMAD2 and p-SMAD3) and of the TGF- β target gene CTGF (Figure 5A). Moreover, myCAFs had increased nuclear localization of the TGF- β effector SMAD4 compared to quiescent PSCs and iCAFs (Figure 5B). Consistent with these observations, TGF- β treatment of PSCs cultured in Matrigel in control media did not induce the iCAF phenotype (Supplementary Figure S6A). On the contrary, TGF- β induced the expression of TGF- β responsive genes (e.g. *Ctgf* and collagen type 1, alpha 1 *Col1a1*) and promoted PSC proliferation and morphological changes, in agreement with previous literature (41,42) (Supplementary Figure S6A, S6B and S6C). Accordingly, single cell RNA-sequencing analysis of KPC tumors confirmed higher expression of TGF- β responsive genes in

myCAFs compared to iCAFs *in vivo* (Figure 5C). Moreover, immunofluorescence of p-SMAD2 and E-cadherin (ECAD) showed increased p-SMAD2 levels in cells proximal to ECAD-positive epithelial cells compared to distal areas in KPC tumors (Supplementary Figure S6D). Finally, immunofluorescence co-stain of p-SMAD2 and α SMA in KPC tumors and human PDAC showed elevated number of p-SMAD2/ α SMA double positive myofibroblasts (Figure 5D; Supplementary Figure S6E), which represented the majority of p-SMAD2-positive cells (Figure 5E; Supplementary Figure S6F). Altogether these results suggest that TGF- β signaling is active in myCAFs in mouse and human PDAC.

As tumor-secreted IL-1 should be able to signal to both the distally located iCAFs and the tumor-proximal myCAFs, we reasoned that in myCAFs some other signaling pathway likely prevents the induction of an inflammatory phenotype. Accordingly, the observation that nuclear p-STAT3 is rarely found in α SMA-positive myCAFs surrounding cancer cells (Figure 4H) is consistent with a role for tumor-proximal paracrine or juxtacrine signaling in preventing JAK/STAT activation and the iCAF phenotype. Given that TGF- β signaling was more active in myCAFs compared to iCAFs (Figure 5A, 5B and 5C), we tested whether TGF- β signaling might be responsible for the inhibition of the iCAF phenotype in myCAFs. Indeed, treatment of PSCs cultured to form iCAFs with the TGF- β pathway inhibitor A83-01 led to increased expression of iCAF marker genes (Supplementary Figure S6G). Congruent with the hypothesis that TGF- β signaling inhibits iCAF formation, addition of TGF- β to tumor organoid-conditioned media or to media containing IL-1 α significantly reduced the expression of iCAF markers and partially increased myofibroblastic markers in mouse and human PSCs (Figure 5F; Supplementary Figure S6H and S6I). Accordingly, addition of TGF- β blocked the activation of JAK/STAT signaling in PSCs cultured with tumor organoid-conditioned media or IL-1 α (Figure 5G; Supplementary Figure S6J), suggesting that the downregulation of iCAF gene expression observed is a consequence of TGF- β -mediated inhibition of the JAK/STAT pathway. Proliferation assays showed that myCAFs proliferate faster than iCAFs *in vitro* (Supplementary Figure S6K). Consistent with the hypothesis that TGF- β shifts the iCAF phenotype to a more myofibroblastic state, the proliferation rate of PSCs cultured with tumor organoid-conditioned media containing TGF- β was higher than PSCs cultured in conditioned media alone (Figure 5H).

We have shown that JAK/STAT signaling positively regulates the expression of IL-1R1 (Figure 4G; Supplementary Figure S5M and S5N). To further investigate the molecular mechanism behind TGF- β and JAK/STAT pathway antagonism in the context of CAF heterogeneity in PDAC, we performed DNA motif analysis and found, in addition to STAT3 motifs, SMAD2/3/4 motifs in the promoters of both mouse and human *Il1r1* genes ($p < 0.001$; Supplementary Table S1). In addition, analysis of human SMAD3 ChIP-seq datasets confirmed SMAD3 binding at the *IL1R1* promoter (43). We therefore hypothesized that TGF- β antagonizes JAK/STAT signaling by directly repressing *Il1r1* expression and thus blocking the cytokine cascade triggered downstream of IL-1R1 activation. To test our hypothesis, we measured *Il1r1* expression levels following TGF- β treatment in PSCs cultured with control media or tumor organoid-conditioned media and demonstrated that TGF- β treatment significantly reduced IL-1R1 expression (Figure 5I and 5J). Similar results were obtained with mouse and human PSCs cultured with both IL-1 α and TGF- β (Supplementary Figure S6L and S6M). These results demonstrate that TGF- β inhibits the

iCAF phenotype by downregulating IL-1R1 expression. Altogether, these data suggest that TGF- β prevents activation of the iCAF phenotype by removing the receptor that would activate the cascade that leads to iCAF formation.

TGF- β signaling inhibition targets myCAFs *in vivo*

To evaluate the role of TGF- β signaling in myCAFs *in vivo*, we treated tumor-bearing KPC mice for 10 days with the TGF- β receptor (TGFBR) inhibitor Galunisertib (LY2157299) (44). Assessment of p-SMAD2 levels confirmed effective targeting of the TGF- β pathway (Supplementary Figure S7A and S7B). Treated mice showed a modest reduction in tumor cell proliferation (Supplementary Figure S7C and S7D), but no change in tumor growth (Figure 6A). Additionally, stromal content was modestly, yet significantly reduced, demonstrating attenuation of myCAF properties, as shown by the analysis of collagen deposition (Figure 6B, 6C and 6D) and α SMA levels (Figure 6E and 6F). While Galunisertib did not significantly increase the iCAF content of treated KPC mice (Supplementary Figure S7E and S7F), our results collectively support a key role of the TGF- β pathway in myCAFs *in vivo*.

JAK inhibition shifts iCAFs to a myofibroblastic phenotype *in vivo*

Finally, to determine the role of JAK/STAT signaling in CAFs *in vivo*, we treated tumor-bearing KPC mice with the JAK inhibitor AZD1480 for 10 days. Assessment of p-STAT3 levels confirmed inhibition of the JAK/STAT pathway (Supplementary Figure S8A and S8B). Contrary to what observed following inhibition of TGF- β signaling, tumor volume analysis revealed a significant decrease in tumor growth following treatment with the JAK inhibitor compared to vehicle (Figure 7A). This reduction in tumor growth was associated with impaired proliferation of cancer cells in the treated tumors, as shown by quantification of p-H3 levels (Supplementary Figure S8C and S8D). Histologically, this treatment led to a significant increase in collagen deposition (Figure 7B, 7C and 7D). Flow cytometry analysis of KPC tumors using our previously described strategy (Supplementary Figure S1B) also revealed increased abundance of CAFs in JAK inhibitor-treated tumors compared to vehicle controls (Figure 7E; Supplementary Figure S8E). Moreover, KPC tumors from mice treated with the JAK inhibitor had increased levels of α SMA (Figure 7F and 7G), suggesting that JAK inhibition may promote a shift in the CAF population from an iCAF phenotype towards a more myofibroblastic state.

We previously showed that myCAFs proliferate faster than iCAFs *in vitro* (Supplementary Figure S6K). To explain the increased CAF abundance in JAK inhibitor-treated tumors compared to controls and considering that JAK inhibition seems to promote formation of myofibroblasts, we investigated whether myCAFs proliferate more than iCAFs *in vivo*. Single cell RNA-sequencing analysis of iCAFs and myCAFs in KPC tumors showed higher expression of the cell cycle genes *Cks2* and *Ccnb2* and of the proliferation marker *Mki67* in myCAFs relative to iCAFs (Supplementary Figure S8F). Moreover, we used our flow cytometry strategy with the iCAF marker Ly6C (Supplementary Figure S3K and S3L) to analyze the cell proliferation of CAFs in 5-Ethynyl-2-deoxyuridine (EdU)-labeled KPC tumors. Greater number of Ly6C- CAFs incorporated EdU compared to Ly6C+ iCAFs, suggesting that myCAFs are more proliferative (Figure 7H). Altogether, these data provide

an explanation for the increased CAF abundance observed in JAK inhibitor-treated KPC tumors (Figure 7E; Supplementary Figure S8E).

To confirm that JAK inhibition increased the number of myfibroblasts, we used the Ly6C-based flow cytometry approach to quantify iCAF and myCAF populations in vehicle- or JAK inhibitor- treated KPC tumors. The results demonstrated reduced presence of Ly6C+ iCAFs in JAK inhibitor-treated tumors compared to vehicle controls (Figure 7I; Supplementary Figure S8G and S8H), further supporting a role for JAK inhibition in modulating the PDAC microenvironment by shifting iCAFs towards a more myofibroblastic state.

Altogether, our data support a model in which pathway antagonism between JAK/STAT and TGF- β signaling acts to define CAF heterogeneity in PDAC. In particular, tumor-secreted TGF- β acts locally on adjacent myCAFs, downregulating the expression of IL-1R1, thereby preventing the IL-1-dependent activation of JAK/STAT signaling. Ultimately, this prevents induction of the iCAF phenotype in tumor-proximal myCAFs. Furthermore, TGF- β , which is secreted as a latent form and sequestered by the extracellular matrix, cannot act on CAFs located distally from tumor glands, leading to increased IL-1R1 expression in these distal CAFs. This allows tumor-secreted IL-1 to stimulate a cytokine cascade following activation of NF- κ B signaling that, predominantly through autocrine LIF, activates the JAK/STAT pathway in CAFs. JAK/STAT signaling then maintains the inflammatory CAF phenotype through a positive feedback loop involving STAT3-mediated upregulation of IL-1R1 (Figure 7J).

DISCUSSION

Here, we have identified TGF- β and IL-1/JAK/STAT signaling as the major pathways responsible for myCAF and iCAF formation in mouse and human PDAC and organoid models. Notably, gene set enrichment analysis of iCAF and myCAF populations that have been identified by single cell RNA-sequencing in human PDAC samples has confirmed that JAK/STAT pathway is significantly upregulated in iCAFs compared to myCAFs (Elyada et al. in preparation). Additionally, in agreement with our previous work (19), we identified a minor population of α SMA/p-STAT3 double positive cells by immunofluorescence. These cells might represent an additional subtype of CAFs or an intermediate state between the iCAF and myCAF phenotype, supporting the potential plasticity between these two cell subtypes *in vivo* and recapitulating what was observed *in vitro* (19). We suggest that iCAFs and myCAFs are indeed interconvertible cell states, rather than endpoints in differentiation, depending on their location within the tumor and on the tumor-derived cues they are exposed to. This could direct the design of treatment strategies meant to convert potential tumor-promoting CAFs into tumor-restraining CAF populations. The secretory phenotype of iCAFs suggest a role for this CAF subtype in promoting tumor progression, chemoresistance and other cancer-associated systemic effects, such as cachexia and immune suppression (6,9,11,21-24,38,45,46). The benefits of targeting iCAFs would be two-fold: depleting iCAFs would reduce the secretion of tumor-promoting cytokines and chemokines, and shifting iCAFs to a more myofibroblastic state would increase the α SMA-positive CAF population that has been previously suggested to restrain tumor progression (14,16).

Accordingly, JAK inhibition significantly increased the myCAF/iCAF ratio in treated tumors. This was also reflected in an extensive deposition of extracellular matrix, a feature attributed to myCAFs, which by acting as a barrier to drug delivery would offer a potential explanation for the poor outcome observed in clinical trials using JAK inhibitors with chemotherapy (47,48). Although the dramatic changes in stromal composition that we observed were not reported in a previous study (49), the different genetics of the PDAC mouse models employed might explain this discrepancy. While we only observed a modest increase in collagen deposition and α SMA levels in orthotopic tumors grown in the IL-1R1 knockout mouse model compared to control mice, this may reflect the diminished stromal content in this model compared to the KPC mouse model.

Our studies suggest the potential of novel therapeutic combinations to selectively modulate the PDAC stroma by targeting potential tumor-promoting components, such as iCAFs, along with components that impede drug delivery, such as myCAF-derived desmoplasia (2,4,5), while not directly depleting tumor-restraining myCAFs. The potential benefit of targeting iCAFs in PDAC is supported by the observation that a 10-day treatment with the JAK inhibitor in KPC mice led to a significant reduction in cell proliferation and tumor growth, parallel to an increase in the proportion of CAFs as myofibroblasts. On the contrary, TGFBR inhibition did not reduce tumor growth, while partially attenuating the function of myCAFs, suggesting that distinct CAF populations impart differential outcomes on PDAC progression. Although we cannot exclude that these effects on CAF populations are also partially a consequence of direct targeting of cancer cells, these results show differential responses of KPC tumors to drugs that target iCAFs or myCAFs.

Alternative approaches to target the iCAF population are suggested by the identification of IL-1 signaling as the initiator of the cytokine cascade that leads to JAK/STAT activation. Previous studies have reported a role of tumor-secreted IL-1 in remodeling PDAC stroma (32,33). In particular, IL-1 α has been shown to induce the expression of inflammatory factors, such as IL-6 and CXCL8, in PDAC CAFs *in vitro*, although no downstream mechanism has been reported (32). Targeting IL-1 signaling in PDAC mouse models with the IL-1 receptor antagonist Anakinra has shown a role for this pathway in cancer cells in PDAC progression (31), and these preclinical studies have encouraged an early phase 1 clinical trial in combination with standard chemotherapy in PDAC (NCT02021422). Although the effects of IL-1 signaling inhibition in PDAC have been attributed to the role of this pathway in cancer cells, our data suggest that the benefits of the IL-1 receptor antagonist might also depend on targeting of the tumor-supportive inflammatory stroma. We have identified the presence of the IL-1 pathway in a subset of CAFs that, in addition of being uniquely characterized by an inflammatory signature, also features a lack of myofibroblastic features. The combination of these traits might be important for the function of this CAF subtype. In addition, since we demonstrated that LIF is a key mediator of the mechanism that leads to iCAF formation, targeting of the iCAF population might also be achieved by *in vivo* neutralization of LIF. Finally, we have demonstrated that TNF- α has the potential of inducing iCAFs and, therefore, a combinatorial therapy with both a TNF- α neutralizing antibody and the IL-1 receptor antagonist might be necessary for more effective targeting of iCAFs *in vivo*.

Altogether, our observations support a model for myCAF and iCAF formation in which tumor-secreted TGF- β acts locally on the adjacent myCAFs and antagonizes tumor-secreted IL-1 activity and the JAK/STAT pathway. Pathway antagonism between TGF- β and STAT activation has been previously suggested in the context of epithelial cells (50,51). We have now uncovered a role of TGF- β in blocking JAK/STAT signaling in CAFs and we present evidence that this antagonism depends on their opposite effects on IL-1R1 expression. Our study thus explains the mutual exclusivity and plasticity of iCAF and myCAF populations, and provides a platform for further investigation of their role in PDAC progression by selective therapeutic targeting of each population.

METHODS

Mouse models.

KPC (*Kras*^{LSL-G12D/+}; *Trp53*^{LSL-R172H/+}; *Pdx1*-Cre) mice were previously described (18). C57BL/6J (stock number 000664) and IL-1R1 knockout (36)(stock number 003245) mice were purchased from The Jackson Laboratory; nu/nu mice (stock number 24102242) were purchased from Charles River Laboratory. All animal procedures and studies were conducted in accordance with the Institutional Animal Care and Use Committee (IACUC) at CSHL.

Cell lines and cell culture.

Mouse PSCs, KPC primary tumor cells, tumor and metastatic pancreatic organoid lines were previously described (17,19). Primary mouse IL-1R1 knockout PSCs were isolated by IL-1R1 knockout mice, as previously described (19). Human PSCs were purchased from ScienCell (3830, ScienCell). Mouse PSCs, human PSCs, NIH-3T3 fibroblasts (available at CSHL) and KPC primary tumor cells were cultured in DMEM (10-013-CV, Fisher Scientific) containing 5% FBS. All cells were cultured for no more than 20-25 passages at 37°C with 5% CO₂. For conditioned media experiments, tumor organoids were cultured for 3-4 days in DMEM with 5% FBS. For transwell cultures, organoids were plated on top of trans-well membranes (82051-572, VWR) with PSCs growing in Matrigel (356231, Corning) in 24-well plates. Cell lines were characterized by flow cytometry. Cell line authentication was not performed. Mycoplasma testing with MycoAlert Mycoplasma Detection Kit (LT07-318, Lonza) is performed monthly at our institution and each cell line has been tested at least once after thawing or isolation, and re-tested prior RNA-sequencing and orthotopic transplantation experiments.

Drug and antibody treatments.

Cells were treated with 0.1 or 1 ng/mL mouse (400-ML-005/CF, R&D Systems) or human (200-LA-002/CF, R&D Systems) IL-1 α , 1 ng/mL mouse IL-1 β (401-ML-005/CF, R&D Systems), 10 ng/mL mouse TNF- α (410-MT-010/CF, R&D Systems), 20 ng/mL mouse (7666-MB-005/CF, R&D systems) or human TGF- β 1 (T7039-2UG, Sigma), 500 nM JAK inhibitor AZD1480 (S2162, Selleck Chem), 30 μ M IKK- β inhibitor ML102B, 1 μ M A83-01 (2939, Tocris Bioscience), 3 μ g/mL IL-1 α neutralizing antibody (MAB4001, R&D Systems) or an IgG control (400902, Biolegend), 5 μ g/mL TNF- α neutralizing antibody (11969S, Cell signaling) or an IgG control (sc-2027, Santa Cruz), 3.4 μ g/mL LIF neutralizing antibody

(AF449, R&D Systems) or an IgG control (AB-108-C, R&D), 3.8 µg/mL G-CSF (MAB414, R&D Systems) or IL-6 (MAB406, R&D Systems) neutralizing antibodies or an IgG control (MAB005, R&D).

IL-1R1, LIF, STAT3, STAT1 and IL-1α CRISPR/Cas9 knockout.

To knock out IL-1R1, STAT3, STAT1 and LIF in PSCs, lenti-Cas9-Blast plasmids (52962, Addgene) were used. PSCs were infected and selected using 2 µg/ml blasticidin (A11139-03, Thermo Fisher Scientific). Short guide RNAs (sgRNAs) were designed using CRISPR Design (<http://crispr.mit.edu>) and cloned into the LRGF (Lenti-sgRNA-EFS-GFP-neo) plasmid. Cleavage was confirmed using the GeneArt Genomic Cleavage Detection Kit (A24372, Invitrogen). PSCs were plated as single clones in 96-well plates in the presence of neomycin (10131035, Invitrogen). Generation of IL-6 KO PSCs was previously described (19). To knock out IL-1α in tumor organoids, LentiV_Cas9_puro plasmids were used. Tumor organoids were infected and selected using 2.5 µg/ml puromycin (A1113803, Thermo Scientific). sgRNAs were designed, cloned and validated as above. Organoids were infected and plated as single cells in the presence of neomycin. Knockout was confirmed by Sanger sequencing and western blot analysis or ELISA. gRNA-resistant IL-1R1 cDNA was generated by site-directed mutagenesis of the gRNA PAM sequence using the QuikChange Lightning Site-Directed Mutagenesis kit (210515, Agilent). Wild-type mouse IL-1R1 cDNA (MC219163, Origene) was PCR amplified with mutagenic primers to induce a G>T transversion, thereby converting codon 8 from GGG>GGT.

qPCR analysis.

1 µg RNA was reverse transcribed using TaqMan reverse transcription reagents (N808-0234, Applied Biosystems). qPCR was performed using gene-specific TaqMan probes (Applied Biosystems) and master mix (4440040, Applied Biosystems). Gene expression was normalized to *Hprt*.

Nuclear fractionation.

PSCs were harvested in Cell Recovery Solution (354253, Corning) and incubated rotating for 30 min at 4°C. Pellets were lysed with 10 mM Tris pH 8.0, 10 mM NaCl and 0.2% NP-40, incubated on ice for 15 min and spun down. Supernatants containing cytoplasmic fractions were collected. Pellets were resuspended in 50 mM Tris pH 8.0, 10 mM EDTA and 1% SDS, incubated on ice for 10 min, sonicated and spun down at max speed for 15 min. Supernatants containing nuclear fractions were collected.

Western blot analysis.

PSCs and organoids were harvested in Cell Recovery Solution and incubated rotating for 30 min at 4°C. Cells were pelleted, and lysed in 0.1% Triton X-100, 15 mM NaCl, 0.5 mM EDTA, 5 mM Tris, pH 7.5, supplemented with protease Mini-complete protease inhibitors (11836170001, Roche) and a phosphatase inhibitor cocktail (4906845001, Roche). Cells were incubated on ice for 30 min before clarification. Standard procedures were used for western blotting. Primary antibodies used were: αSMA (M0851, Dako), HSP90α (07-2174, EMD Millipore), ACTIN (8456, Cell Signaling Technology), STAT3 (9139, Cell Signaling

Technology), p-STAT3 (9145, Cell Signaling Technology), STAT1 (9172, Cell Signaling Technology), p-STAT1 (9167, Cell Signaling Technology), IL-1R1 (AF771, R&D Systems), p-JAK1 (3331, Cell Signaling Technology), JAK1 (MAB42601-SP, R&D), p-JAK2 (3771, Cell Signaling Technology), JAK2 (3230, Cell Signaling Technology), p-p65 (3033, Cell Signaling Technology), p65 (8242, Cell Signaling Technology), H3 (ab4729, Abcam), SMAD4 (sc-7966, Santa Cruz), SMAD2 (5339, Cell Signaling Technology), p-SMAD2 (8828, Cell Signaling Technology), SMAD3 (9513, Cell Signaling Technology), p-SMAD3 (9530, Cell Signaling Technology), CTGF (ab125943, Abcam), I κ B α (4814, Cell Signaling Technology), p-I κ B α (9246, Cell Signaling Technology). Proteins were detected using HRP-conjugated secondary antibodies (Jackson ImmunoResearch Laboratories).

ELISA and Luminex assays.

For ELISA of media, cultures were grown for 4-5 days. Media was collected, spun down and assayed using the manufacturer's protocol. ELISA assays used were: TNF- α (MTA00B, R&D Systems) and IL-1 α (MLA00, R&D Systems). A Milliplex Mouse Cytokine/Chemokine MAGNETIC BEAD Premixed 32 Plex Kit (MCYTMAg-70K-PX32, EMD Millipore) was run on a MAGPIX (MAGPIX-XPONENT, Luminex) to detect G-CSF, IL-6 and LIF.

Proliferation assays.

For proliferation assays of PSCs in Matrigel, 6,000 PSCs were plated in 52 μ l of 50% Matrigel in PBS on white 96-well plates (136101, Corning) and cultured in 100 μ l of media. For proliferation assays in monolayer, 500 PSCs were plated on white 96-well plates and cultured in 100 μ l of DMEM with 5% FBS. For proliferation assays of organoids, 700 single cells were plated on white 96-well plates in 200 μ L of 10% Matrigel in DMEM with 5% FBS. Proliferation was followed for 5-6 days with CellTiter-Glo (G7573, Promega), with measurements every 24 h.

Immunofluorescence and immunohistochemistry staining of tissues.

Human PDAC tissues were purchased from US Biomax, which collects all human tissues under HIPPA approved protocols (HPan-Ade060CS-01, US Biomax). Standard procedures were used for immunohistochemistry and immunofluorescence (IF) staining. Primary antibodies for IF were: p-STAT3, p-SMAD2 (3108, Cell Signaling Technology), α SMA (M0851, Dako) and E-cadherin (610181, BD Biosciences). Secondary antibodies were anti-mouse Alexa Fluor 568 (A10037, Thermo Fisher Scientific) and HRP anti-rabbit (PI1000, Vector Laboratories). The Perkin Elmer TSA Fluorescein System was used to detect p-STAT3 or p-SMAD2 (NEL701A001KT for mouse and human p-SMAD2 and mouse p-STAT3, and NEL744001KT for human p-STAT3). DAPI (D8417, Sigma-Aldrich) was used as counterstain. Sections were mounted with Prolong Gold antifade reagent (P10144, Invitrogen). Primary antibodies for immunohistochemistry were: p-STAT3, p-SMAD2, E-cadherin, α SMA (ab5694, Abcam), p-H3 (9701, Cell Signaling Technology). For sequential immunohistochemistry, DAB (SK-4105, Vector Laboratories) and VIP (SK-4605, Vector Laboratories) were used for different primary antibodies. Hematoxylin was used as nuclear counterstain. Hematoxylin and Eosin (H&E) and Masson's trichrome stainings were performed according to standard protocols. Fluorescence imaging of tissue was done with a

Leica TCS SP8 laser scanning confocal (Boulder Grove Il), controlled by the LAS AF 3.3.10134 software. Immunofluorescence images were quantified using the population analysis module in Volocity (Improvision, Lexington, MA). Bright field images of tissue slides were obtained with an Axio Imager.A2 (ZEISS). Stained sections were scanned with Aperio ScanScope CS and analyzed using the ImageScope Positive Pixel Count algorithm. To quantify Masson's trichrome stain, hue values for blue and pink were measured using an average hue value of 0.6 and a hue width of 0.854. Percent collagen area was then determined by calculating percentage of blue pixels relative to the entire stained area. To quantify α SMA stain, the percentage of strong positive pixels was calculated relative to the entire section with the ImageScope software. To quantify p-STAT3, p-SMAD2 and p-H3, the percentage of strong positive nuclei was calculated relative to the total number of nuclei with the ImageScope nuclear v9 algorithm.

***In vivo* orthotopic transplantations.**

Orthotopic injections were conducted as previously described (17). 2.5×10^5 cells prepared from organoid cultures were resuspended as a 45 μ l suspension of 50% Matrigel in PBS and injected into the pancreas. Rosa26-targeted and IL-1 α knockout tumors were imaged using the Vevo 3100 Ultrasound at two different orientations with respect to the transducer. Tumor volumes were measured at two angles using the Vevo LAB software program (version 2.2.0).

AZD1480 and LY2157299 treatment in KPC mice.

KPC mice were subjected to high-contrast ultrasound imaging using a Vevo 3100 Ultrasound with a MS250X transducer (FUJIFILM VisualSonics). Mice with tumor diameters of 6-7 mm were randomized and enrolled one day after scanning. The JAK inhibitor AZD1480 was prepared daily as a suspension in 0.1% Tween80, 0.5% hydroxyl propyl methyl cellulose in sterile water. Mice were administered vehicle or 50 mg/kg of AZD1480 for 10 days, once a day via oral gavage. The TGFBR inhibitor Galunisertib (LY2157299) was prepared daily as a suspension in 0.5% hydroxyl propyl methyl cellulose in sterile water. Mice were administered vehicle or 75 mg/kg of LY2157299 for 10 days, twice a day via oral gavage. Tumors were imaged using the Vevo 3100 Ultrasound at two different orientations with respect to the transducer. Tumor volumes were measured at two angles, if possible, using the Vevo LAB software program (version 2.2.0).

Flow cytometry and cell sorting.

For sorting of cancer cells and CAFs, KPC tumors were processed as previously described (19). Cells were stained with anti-mouse CD45-AlexaFluor 647 (103124, BioLegend), CD326 (Ep-CAM)-AlexaFluor 488 (118212, BioLegend), CD31-AlexaFluor 647 (102416, Biolegend), CD140a (PDGFR α)-PE (135905, BioLegend), PDPN-APC/Cy7 (127418, Biolegend) and DAPI for 15 min. Cells were sorted on the FACS Aria cell sorter (BD) for DAPI/CD45/CD31- EpCAM+ and DAPI/CD45/CD31/EpCAM- PDPN+ cell populations. For flow cytometry analysis of EdU-treated KPC tumors, KPC mice were administered 300 μ g 5-Ethynyl-2-deoxyuridine (EdU) (61135-33-9, Santa Cruz) formulated in sterile saline twice a day for 3 days via intraperitoneal injection. EdU was detected using Click-iTTM Plus EdU Alexa FluorTM 647 Flow Cytometry Assay Kit (C10634, Thermo Fisher Scientific). For

flow cytometric analysis of IL-1R1 and myCAF/iCAF populations, antibodies employed were: anti-mouse CD31-PE/Cy7 (102418, Biolegend), CD45-PerCP/Cy5.5 (103132, Biolegend), CD326 (Ep-CAM)-AlexaFluor 488, PDPN-APC/Cy7, CD140a (PDGFR α)-PE, Ly6C-APC (128015, Biolegend), biotinylated CD121a (IL-1R, Type I/p80) (113503, Biolegend) and APC Streptavidin (405207, Biolegend).

RNA-sequencing library construction and analysis.

Samples were collected in 1 ml of TRIzol Reagent (15596-018, Thermo Fisher Scientific). RNA was extracted using the PureLink RNA mini kit (12183018A, Thermo Fisher Scientific). RNA quality was assessed on a bioanalyzer using the Agilent RNA 6000 Nano kit (5067-1511, Agilent). We used TruSeq Stranded Total RNA Kit with RiboZero Human/Mouse/Rat (RS-122-2202, Illumina) (0.2-1 μ g per sample, RIN > 8) and proceeded to library preparation using Illumina TruSeq RNA prep kit (IP-202-1012 and IP-202-1024, Illumina). Libraries were then sequenced using Illumina NextSeq500. All RNA-sequencing data are available at Gene Expression Omnibus (GEO) under the accession number GSE113615. Protein coding genes expressed in at least two samples were included for differential expression analysis (DEA). DEA was performed using DESeq program (V2) with default parameters. Genes with adjusted p-values < 0.05 were selected as significantly changed between conditions. The principle components for variance stabilized data were estimated using plotPCA function available in DESeq and plotted using the ggplot2 function in R. Gene set enrichment analysis was performed using the GSEA program (Broad Institute) on the C2 canonical pathway collection (C2.cp.v5.1) downloaded from the Molecular Signatures Database (MSigDB). Genes were ranked by their p-values before submitted to GSEA for analysis.

STAT3 and SMAD2/3/4 motif searching.

STAT3 and SMAD2/3/4 human and mouse motif position weight matrices (PWMs) were downloaded from JASPAR 2018 database. Promoter sequences (–5 kbp/200 bp surround TSSs) were prepared by custom R and Shell scripts for both hg19 and mm10 genomes. Motif searching was performed using FIMO program available in MEME Suite with p-value < 1e4 as hit cutoff.

Single cell RNA-sequencing of KPC tumors.

Tumors were digested as previously described (19). Single-cell barcoded cDNA libraries were generated using the 10X Genomics Chromium Controller via the Single Cell 3' Library Kit (120237, 10X Genomics). Libraries were sequenced on a NextSeq500 (Illumina). Library batches were normalized using the CellRanger Aggregate function, and the resulting gene-barcode matrices were fed into SCANPY (52). Dimensionality reduction was carried out in SCANPY via principal component analysis followed by Louvain clustering t-SNE visualization using the top 20 significant components. Major clusters were denoted by differentially expressed canonical marker genes, and these were subjected to additional rounds of cluster refinement. All single cell RNA-sequencing data are available at GEO under the accession number GSE114417. Differential expression analysis was performed using SCDE program (53). Differentially expressed genes (adjusted p-values < 0.05) were ranked by Z scores reported by SCDE and submitted to GSEA program (54). DE genes were

compared to their counterparts from a bulk RNASeq dataset (19). Overlap p-values were calculated using *phyper* function in R. Venny program was used to produce the Venn diagrams. To generate heatmaps, the pre-processed data matrices were passed from SCANPY to the Seurat package (PMCID: PMC4430369), and marker genes discriminating the fibroblast subpopulations were identified using the FindMarkers function. The top 25 markers ranked by Bonferroni adjusted p-values are displayed on a log (10) fold-change color scale, normalized across all cells.

Statistics.

GraphPad Prism was used for graphical representation of data. Statistical analysis was performed using Student's *t* test.

Supplementary Material

Refer to Web version on PubMed Central for supplementary material.

Acknowledgments

The authors would like to thank the Cold Spring Harbor Cancer Center Support Grant (CCSG) shared resources: Bioinformatics Shared Resource, Next Generation Sequencing Core Facility, P. Moody and C. Kanzler in the Flow Cytometry Facility, Animal & tissue imaging, and the Animal Facility. The CCSG is funded by the NIH Cancer Center Support Grant 5P30CA045508. We thank Dr. L. Baker for critical review of the manuscript. We thank Dr. J. Ipsaro for the initial biochemical characterization of tumor organoid-conditioned media. We thank Dr. F. Greten for kindly providing us with ML102B. This work was supported by the Lustgarten Foundation, where D.A. Tuveson is a distinguished scholar and Director of the Lustgarten Foundation-designated Laboratory of Pancreatic Cancer Research. D.A. Tuveson is also supported by the Cold Spring Harbor Laboratory Association and the National Institutes of Health (NIH 5P30CA45508, 5P50CA101955, P20CA192996, U10CA180944, U01CA210240, U01CA224013, 1R01CA188134 and 1R01CA190092). In addition, we are grateful for support from the following: the Human Frontiers Science Program (LT000195/2015-L for G. Biffi and LT000403/2014-L for E. Elyada), EMBO (ALTF 1203-2014 for G. Biffi), The Northwell Health Affiliation (for J. Preall and D.A. Tuveson) and the (NIH R50 CA211506 for Y. Park).

References

1. Siegel RL, Miller KD, Jemal A. Cancer statistics, 2016. *CA Cancer J Clin* 2016;66(1):7–30 doi 10.3322/caac.21332. [PubMed: 26742998]
2. Jacobetz MA, Chan DS, Neesse A, Bapiro TE, Cook N, Frese KK, et al. Hyaluronan impairs vascular function and drug delivery in a mouse model of pancreatic cancer. *Gut* 2013;62(1):112–20 doi 10.1136/gutjnl-2012-302529. [PubMed: 22466618]
3. Olive KP, Jacobetz MA, Davidson CJ, Gopinathan A, McIntyre D, Honess D, et al. Inhibition of Hedgehog signaling enhances delivery of chemotherapy in a mouse model of pancreatic cancer. *Science* 2009;324(5933):1457–61 doi 10.1126/science.1171362. [PubMed: 19460966]
4. Provenzano PP, Cuevas C, Chang AE, Goel VK, Von Hoff DD, Hingorani SR. Enzymatic targeting of the stroma ablates physical barriers to treatment of pancreatic ductal adenocarcinoma. *Cancer Cell* 2012;21(3):418–29 doi 10.1016/j.ccr.2012.01.007. [PubMed: 22439937]
5. Diop-Frimpong B, Chauhan VP, Krane S, Boucher Y, Jain RK. Losartan inhibits collagen I synthesis and improves the distribution and efficacy of nanotherapeutics in tumors. *Proc Natl Acad Sci U S A* 2011;108(7):2909–14 doi 10.1073/pnas.1018892108. [PubMed: 21282607]
6. Hwang RF, Moore T, Arumugam T, Ramachandran V, Amos KD, Rivera A, et al. Cancer-associated stromal fibroblasts promote pancreatic tumor progression. *Cancer Res* 2008;68(3):918–26 doi 10.1158/0008-5472.CAN-07-5714. [PubMed: 18245495]
7. Long KB, Tooker G, Tooker E, Luque SL, Lee JW, Pan X, et al. IL6 Receptor Blockade Enhances Chemotherapy Efficacy in Pancreatic Ductal Adenocarcinoma. *Mol Cancer Ther* 2017;16(9):1898–908 doi 10.1158/1535-7163.MCT-16-0899. [PubMed: 28611107]

8. Singh S, Srivastava SK, Bhardwaj A, Owen LB, Singh AP. CXCL12-CXCR4 signalling axis confers gemcitabine resistance to pancreatic cancer cells: a novel target for therapy. *Br J Cancer* 2010;103(11):1671–9 doi 10.1038/sj.bjc.6605968. [PubMed: 21045835]
9. Straussman R, Morikawa T, Shee K, Barzily-Rokni M, Qian ZR, Du J, et al. Tumour micro-environment elicits innate resistance to RAF inhibitors through HGF secretion. *Nature* 2012;487(7408):500–4 doi 10.1038/nature11183. [PubMed: 22763439]
10. Hessmann E, Patzak MS, Klein L, Chen N, Kari V, Ramu I, et al. Fibroblast drug scavenging increases intratumoural gemcitabine accumulation in murine pancreas cancer. *Gut* 2018;67(3):497–507 doi 10.1136/gutjnl-2016-311954. [PubMed: 28077438]
11. Feig C, Jones JO, Kraman M, Wells RJ, Deonaraine A, Chan DS, et al. Targeting CXCL12 from FAP-expressing carcinoma-associated fibroblasts synergizes with anti-PD-L1 immunotherapy in pancreatic cancer. *Proc Natl Acad Sci U S A* 2013;110(50):20212–7 doi 10.1073/pnas.1320318110. [PubMed: 24277834]
12. Sherman MH, Yu RT, Engle DD, Ding N, Atkins AR, Tiriack H, et al. Vitamin D receptor-mediated stromal reprogramming suppresses pancreatitis and enhances pancreatic cancer therapy. *Cell* 2014;159(1):80–93 doi 10.1016/j.cell.2014.08.007. [PubMed: 25259922]
13. Lee JJ, Perera RM, Wang H, Wu DC, Liu XS, Han S, et al. Stromal response to Hedgehog signaling restrains pancreatic cancer progression. *Proc Natl Acad Sci U S A* 2014;111(30):E3091–100 doi 10.1073/pnas.1411679111. [PubMed: 25024225]
14. Rhim AD, Oberstein PE, Thomas DH, Mirek ET, Palermo CF, Sastra SA, et al. Stromal elements act to restrain, rather than support, pancreatic ductal adenocarcinoma. *Cancer Cell* 2014;25(6):735–47 doi 10.1016/j.ccr.2014.04.021. [PubMed: 24856585]
15. Kim EJ, Sahai V, Abel EV, Griffith KA, Greenson JK, Takebe N, et al. Pilot clinical trial of hedgehog pathway inhibitor GDC-0449 (vismodegib) in combination with gemcitabine in patients with metastatic pancreatic adenocarcinoma. *Clin Cancer Res* 2014;20(23):5937–45 doi 10.1158/1078-0432.CCR-14-1269. [PubMed: 25278454]
16. Ozdemir BC, Pentcheva-Hoang T, Carstens JL, Zheng X, Wu CC, Simpson TR, et al. Depletion of carcinoma-associated fibroblasts and fibrosis induces immunosuppression and accelerates pancreas cancer with reduced survival. *Cancer Cell* 2014;25(6):719–34 doi 10.1016/j.ccr.2014.04.005. [PubMed: 24856586]
17. Boj SF, Hwang CI, Baker LA, Chio II, Engle DD, Corbo V, et al. Organoid models of human and mouse ductal pancreatic cancer. *Cell* 2015;160(1–2):324–38 doi 10.1016/j.cell.2014.12.021. [PubMed: 25557080]
18. Hingorani SR, Wang L, Multani AS, Combs C, Deramaudt TB, Hruban RH, et al. Trp53R172H and KrasG12D cooperate to promote chromosomal instability and widely metastatic pancreatic ductal adenocarcinoma in mice. *Cancer Cell* 2005;7(5):469–83 doi 10.1016/j.ccr.2005.04.023. [PubMed: 15894267]
19. Ohlund D, Handly-Santana A, Biffi G, Elyada E, Almeida AS, Ponz-Sarvisse M, et al. Distinct populations of inflammatory fibroblasts and myofibroblasts in pancreatic cancer. *J Exp Med* 2017;214(3):579–96 doi 10.1084/jem.20162024. [PubMed: 28232471]
20. Bernard V, Semaan A, Huang J, San Lucas FA, Mulu FC, Stephens BM, et al. Single Cell Transcriptomics of Pancreatic Cancer Precursors Demonstrates Epithelial and Microenvironmental Heterogeneity as an Early Event in Neoplastic Progression. *bioRxiv* 2018 doi 10.1101/306134.
21. Albregues J, Bertero T, Grasset E, Bonan S, Maiel M, Bourget I, et al. Epigenetic switch drives the conversion of fibroblasts into proinvasive cancer-associated fibroblasts. *Nat Commun* 2015;6:10204 doi 10.1038/ncomms10204. [PubMed: 26667266]
22. Corcoran RB, Contino G, Deshpande V, Tzatsos A, Conrad C, Benes CH, et al. STAT3 plays a critical role in KRAS-induced pancreatic tumorigenesis. *Cancer Res* 2011;71(14):5020–9 doi 10.1158/0008-5472.CAN-11-0908. [PubMed: 21586612]
23. Lesina M, Kurkowski MU, Ludes K, Rose-John S, Treiber M, Kloppel G, et al. Stat3/Socs3 activation by IL-6 transsignaling promotes progression of pancreatic intraepithelial neoplasia and development of pancreatic cancer. *Cancer Cell* 2011;19(4):456–69 doi 10.1016/j.ccr.2011.03.009. [PubMed: 21481788]

24. Li J, Byrne KT, Yan F, Yamazoe T, Chen Z, Baslan T, et al. Tumor Cell-Intrinsic Factors Underlie Heterogeneity of Immune Cell Infiltration and Response to Immunotherapy. *Immunity* 2018;49(1): 178–93 e7 doi 10.1016/j.immuni.2018.06.006. [PubMed: 29958801]
25. Erez N, Truitt M, Olson P, Arron ST, Hanahan D. Cancer-Associated Fibroblasts Are Activated in Incipient Neoplasia to Orchestrate Tumor-Promoting Inflammation in an NF-kappaB-Dependent Manner. *Cancer Cell* 2010;17(2):135–47 doi 10.1016/j.ccr.2009.12.041. [PubMed: 20138012]
26. Su S, Chen J, Yao H, Liu J, Yu S, Lao L, et al. CD10(+)GPR77(+) Cancer-Associated Fibroblasts Promote Cancer Formation and Chemoresistance by Sustaining Cancer Stemness. *Cell* 2018;172(4):841–56 e16 doi 10.1016/j.cell.2018.01.009. [PubMed: 29395328]
27. Egberts JH, Cloosters V, Noack A, Schniewind B, Thon L, Klose S, et al. Anti-tumor necrosis factor therapy inhibits pancreatic tumor growth and metastasis. *Cancer Res* 2008;68(5):1443–50 doi 10.1158/0008-5472.CAN-07-5704. [PubMed: 18316608]
28. Ling J, Kang Y, Zhao R, Xia Q, Lee DF, Chang Z, et al. KrasG12D-induced IKK2/beta/NF-kappaB activation by IL-1alpha and p62 feedforward loops is required for development of pancreatic ductal adenocarcinoma. *Cancer Cell* 2012;21(1):105–20 doi 10.1016/j.ccr.2011.12.006. [PubMed: 22264792]
29. Melisi D, Niu J, Chang Z, Xia Q, Peng B, Ishiyama S, et al. Secreted interleukin-1alpha induces a metastatic phenotype in pancreatic cancer by sustaining a constitutive activation of nuclear factor-kappaB. *Mol Cancer Res* 2009;7(5):624–33 doi 10.1158/1541-7786.MCR-08-0201. [PubMed: 19435817]
30. Niu J, Li Z, Peng B, Chiao PJ. Identification of an autoregulatory feedback pathway involving interleukin-1alpha in induction of constitutive NF-kappaB activation in pancreatic cancer cells. *J Biol Chem* 2004;279(16):16452–62 doi 10.1074/jbc.M309789200. [PubMed: 14679213]
31. Zhuang Z, Ju HQ, Aguilar M, Gocho T, Li H, Iida T, et al. IL1 Receptor Antagonist Inhibits Pancreatic Cancer Growth by Abrogating NF-kappaB Activation. *Clin Cancer Res* 2016;22(6): 1432–44 doi 10.1158/1078-0432.CCR-14-3382. [PubMed: 26500238]
32. Tjomsland V, Spangeus A, Valila J, Sandstrom P, Borch K, Druid H, et al. Interleukin 1alpha sustains the expression of inflammatory factors in human pancreatic cancer microenvironment by targeting cancer-associated fibroblasts. *Neoplasia* 2011;13(8):664–75. [PubMed: 21847358]
33. Zhang D, Li L, Jiang H, Li Q, Wang-Gillam A, Yu J, et al. Tumor-Stroma IL1beta-IRAK4 Feedforward Circuitry Drives Tumor Fibrosis, Chemoresistance, and Poor Prognosis in Pancreatic Cancer. *Cancer Res* 2018;78(7):1700–12 doi 10.1158/0008-5472.CAN-17-1366. [PubMed: 29363544]
34. Zhao X, Fan W, Xu Z, Chen H, He Y, Yang G, et al. Inhibiting tumor necrosis factor-alpha diminishes desmoplasia and inflammation to overcome chemoresistance in pancreatic ductal adenocarcinoma. *Oncotarget* 2016;7(49):81110–22 doi 10.18632/oncotarget.13212. [PubMed: 27835602]
35. Wen D, Nong Y, Morgan JG, Gangurde P, Bielecki A, Dasilva J, et al. A selective small molecule IkappaB Kinase beta inhibitor blocks nuclear factor kappaB-mediated inflammatory responses in human fibroblast-like synoviocytes, chondrocytes, and mast cells. *J Pharmacol Exp Ther* 2006;317(3):989–1001 doi 10.1124/jpet.105.097584. [PubMed: 16525037]
36. Glaccum MB, Stocking KL, Charrier K, Smith JL, Willis CR, Maliszewski C, et al. Phenotypic and functional characterization of mice that lack the type I receptor for IL-1. *J Immunol* 1997;159(7): 3364–71. [PubMed: 9317135]
37. Phan VT, Wu X, Cheng JH, Sheng RX, Chung AS, Zhuang G, et al. Oncogenic RAS pathway activation promotes resistance to anti-VEGF therapy through G-CSF-induced neutrophil recruitment. *Proc Natl Acad Sci U S A* 2013;110(15):6079–84 doi 10.1073/pnas.1303302110. [PubMed: 23530240]
38. Pickup MW, Owens P, Gorska AE, Chytil A, Ye F, Shi C, et al. Development of Aggressive Pancreatic Ductal Adenocarcinomas Depends on Granulocyte Colony Stimulating Factor Secretion in Carcinoma Cells. *Cancer Immunol Res* 2017;5(9):718–29 doi 10.1158/2326-6066.CIR-16-0311. [PubMed: 28775207]
39. Hedvat M, Huszar D, Herrmann A, Gozgit JM, Schroeder A, Sheehy A, et al. The JAK2 inhibitor AZD1480 potently blocks Stat3 signaling and oncogenesis in solid tumors. *Cancer Cell* 2009;16(6):487–97 doi 10.1016/j.ccr.2009.10.015. [PubMed: 19962667]

40. Fleming JD, Giresi PG, Lindahl-Allen M, Krall EB, Lieb JD, Struhl K. STAT3 acts through pre-existing nucleosome-depleted regions bound by FOS during an epigenetic switch linking inflammation to cancer. *Epigenetics Chromatin* 2015;8:7 doi 10.1186/1756-8935-8-7. [PubMed: 25784959]
41. Evans RA, Tian YC, Steadman R, Phillips AO. TGF-beta1-mediated fibroblast-myofibroblast terminal differentiation-the role of Smad proteins. *Exp Cell Res* 2003;282(2):90–100. [PubMed: 12531695]
42. Vaughan MB, Howard EW, Tomasek JJ. Transforming growth factor-beta1 promotes the morphological and functional differentiation of the myofibroblast. *Exp Cell Res* 2000;257(1):180–9 doi 10.1006/excr.2000.4869. [PubMed: 10854066]
43. Ding N, Yu RT, Subramaniam N, Sherman MH, Wilson C, Rao R, et al. A vitamin D receptor/SMAD genomic circuit gates hepatic fibrotic response. *Cell* 2013;153(3):601–13 doi 10.1016/j.cell.2013.03.028. [PubMed: 2362244]
44. Yingling JM, McMillen WT, Yan L, Huang H, Sawyer JS, Graff J, et al. Preclinical assessment of galunisertib (LY2157299 monohydrate), a first-in-class transforming growth factor-beta receptor type I inhibitor. *Oncotarget* 2018;9(6):6659–77 doi 10.18632/oncotarget.23795. [PubMed: 29467918]
45. Flint TR, Janowitz T, Connell CM, Roberts EW, Denton AE, Coll AP, et al. Tumor-Induced IL-6 Reprograms Host Metabolism to Suppress Anti-tumor Immunity. *Cell Metab* 2016;24(5):672–84 doi 10.1016/j.cmet.2016.10.010. [PubMed: 27829137]
46. Mace TA, Shakya R, Pitarresi JR, Swanson B, McQuinn CW, Loftus S, et al. IL-6 and PD-L1 antibody blockade combination therapy reduces tumour progression in murine models of pancreatic cancer. *Gut* 2018;67(2):320–32 doi 10.1136/gutjnl-2016-311585. [PubMed: 27797936]
47. Hurwitz H, Van Cutsem E, Bendell J, Hidalgo M, Li CP, Salvo MG, et al. Ruxolitinib + capecitabine in advanced/metastatic pancreatic cancer after disease progression/intolerance to first-line therapy: JANUS 1 and 2 randomized phase III studies. *Invest New Drugs* 2018 doi 10.1007/s10637-018-0580-2.
48. Hurwitz HI, Uppal N, Wagner SA, Bendell JC, Beck JT, Wade SM, 3rd, et al. Randomized, Double-Blind, Phase II Study of Ruxolitinib or Placebo in Combination With Capecitabine in Patients With Metastatic Pancreatic Cancer for Whom Therapy With Gemcitabine Has Failed. *J Clin Oncol* 2015;33(34):4039–47 doi 10.1200/JCO.2015.61.4578. [PubMed: 26351344]
49. Nagathihalli NS, Castellanos JA, Shi C, Beesetty Y, Reyzer ML, Caprioli R, et al. Signal Transducer and Activator of Transcription 3, Mediated Remodeling of the Tumor Microenvironment Results in Enhanced Tumor Drug Delivery in a Mouse Model of Pancreatic Cancer. *Gastroenterology* 2015;149(7):1932–43 e9 doi 10.1053/j.gastro.2015.07.058. [PubMed: 26255562]
50. Laklai H, Miroshnikova YA, Pickup MW, Collisson EA, Kim GE, Barrett AS, et al. Genotype tunes pancreatic ductal adenocarcinoma tissue tension to induce matricellular fibrosis and tumor progression. *Nat Med* 2016;22(5):497–505 doi 10.1038/nm.4082. [PubMed: 27089513]
51. Zhao S, Venkatasubbarao K, Lazor JW, Sperry J, Jin C, Cao L, et al. Inhibition of STAT3 Tyr705 phosphorylation by Smad4 suppresses transforming growth factor beta-mediated invasion and metastasis in pancreatic cancer cells. *Cancer Res* 2008;68(11):4221–8 doi 10.1158/0008-5472.CAN-07-5123. [PubMed: 18519681]
52. Wolf FA, Angerer P, Theis FJ. SCANPY: large-scale single-cell gene expression data analysis. *Genome Biol* 2018;19(1):15 doi 10.1186/s13059-017-1382-0. [PubMed: 29409532]
53. Kharchenko PV, Silberstein L, Scadden DT. Bayesian approach to single-cell differential expression analysis. *Nat Methods* 2014;11(7):740–2 doi 10.1038/nmeth.2967. [PubMed: 24836921]
54. Subramanian A, Tamayo P, Mootha VK, Mukherjee S, Ebert BL, Gillette MA, et al. Gene set enrichment analysis: a knowledge-based approach for interpreting genome-wide expression profiles. *Proc Natl Acad Sci U S A* 2005;102(43):15545–50 doi 10.1073/pnas.0506580102. [PubMed: 16199517]

Statement of significance

Understanding the mechanisms that determine CAF heterogeneity in PDAC is a prerequisite for the rational development of approaches that selectively target tumor-promoting CAFs. Here, we identify an IL-1-induced signaling cascade that leads to JAK/STAT activation and promotes an inflammatory CAF state, suggesting multiple strategies to target these cells *in vivo*.

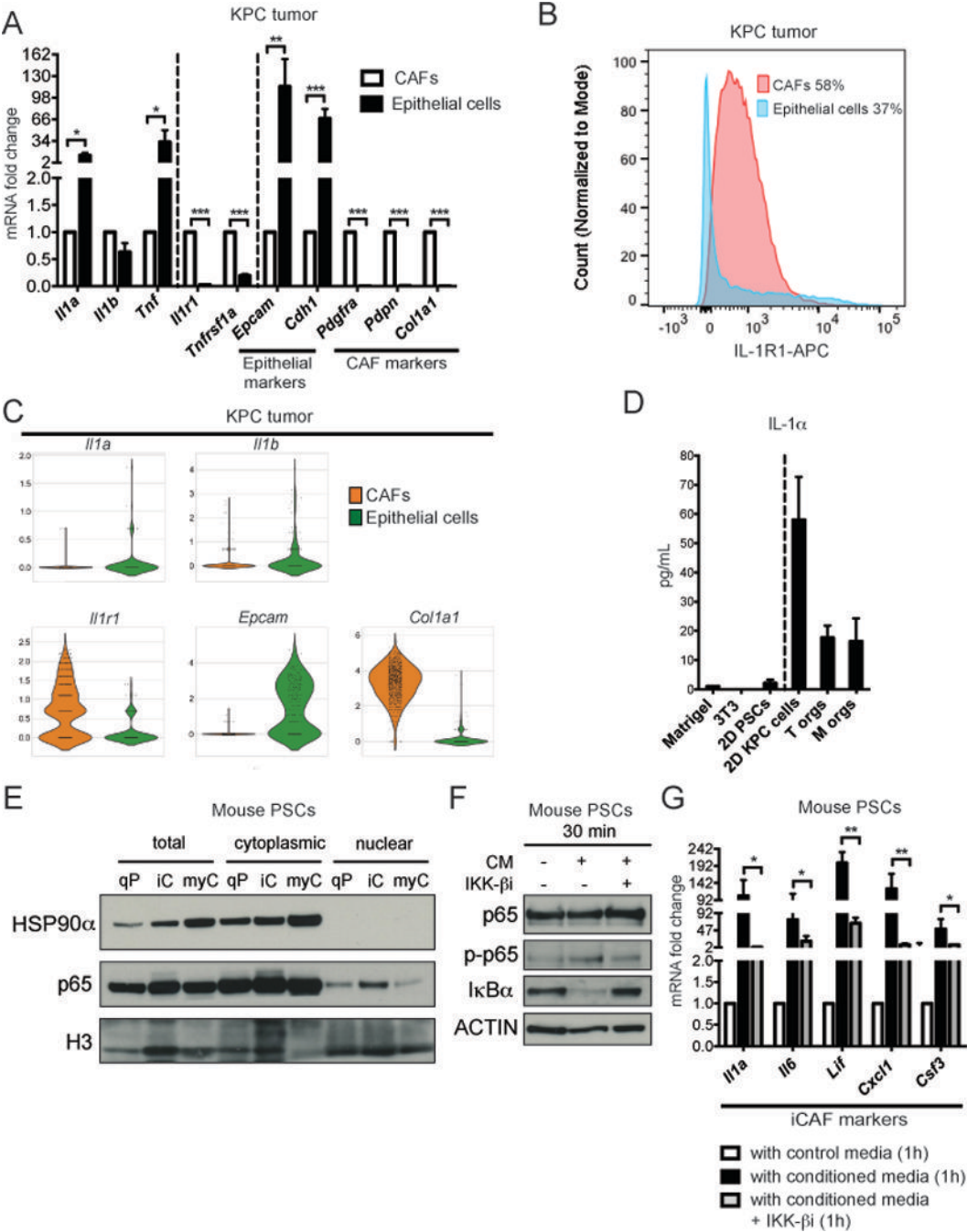


Figure 1: Active NF-κB signaling is associated with the iCAF phenotype.
A. qPCR analysis of *Il1a*, *Il1b*, *Tnf*, *Il1r1*, *Tnfrsf1a*, and epithelial (*Epcam* and *Cdh1*) and fibroblast (*Pdgfra*, *Pdpn* and *Col1a1*) markers in EpCAM+ (epithelial cells) relative to PDPN+ (CAFs) cells sorted from KPC tumors. Results show mean ± SEM (standard error of the mean) of 6 biological replicates. *P<0.05, **P<0.01, ***P<0.001, paired Student's *t* test.
B. Representative flow cytometric analysis of IL-1R1 in EpCAM+ (epithelial cells) and PDPN+ (CAFs) cells in KPC tumors (n=3). Percentages shown were calculated from the parental gate. **C.** Violin plots showing single cell RNA-sequencing analysis of *Il1a*, *Il1b*,

Il1r1, *Epcam* and *Col1a1* of a representative KPC tumor (n=2) in CAFs (orange) and epithelial cells (green). **D.** ELISA of IL-1 α from media of mouse 2D KPC cells (n=2), tumor (T) (n=8) and metastatic (M) (n=8) organoids, and controls that do not induce the iCAF phenotype (n=2 for each control). Results show mean \pm SEM. **E.** Western blot analysis of the nuclear factor NF- κ B p65 subunit following nuclear fractionation of quiescent PSCs (qP, PSCs cultured in Matrigel with control media, i.e. 5% FBS DMEM, for 4 days), iCAFs (iC, PSCs cultured in Matrigel with tumor organoid-conditioned media for 4 days) and myCAFs (myC, PSCs cultured in monolayer with 5% FBS DMEM). Loading controls, HSP90 α (cytoplasmic fractions) and H3 (nuclear fractions). The same amount of protein lysate was loaded in each lane. **F.** Western blot analysis of total and phosphorylated p65 (p-p65) and of total I κ B α in PSCs cultured in Matrigel in control media or tumor organoid-conditioned media (CM) in the presence or absence of 30 μ M IKK- β inhibitor (IKK- β i) ML102B for 30 min. Loading control, ACTIN. **G.** qPCR analysis of iCAF markers (*Il1a*, *Il6*, *Lif*, *Cxcl1* and *Csf3*) in PSCs cultured in Matrigel with control media or tumor organoid-conditioned media for 1 h in the presence or absence of 30 μ M ML102B. Results show mean \pm SEM of 3 biological replicates. *P<0.05, **P<0.01, paired Student's *t* test.

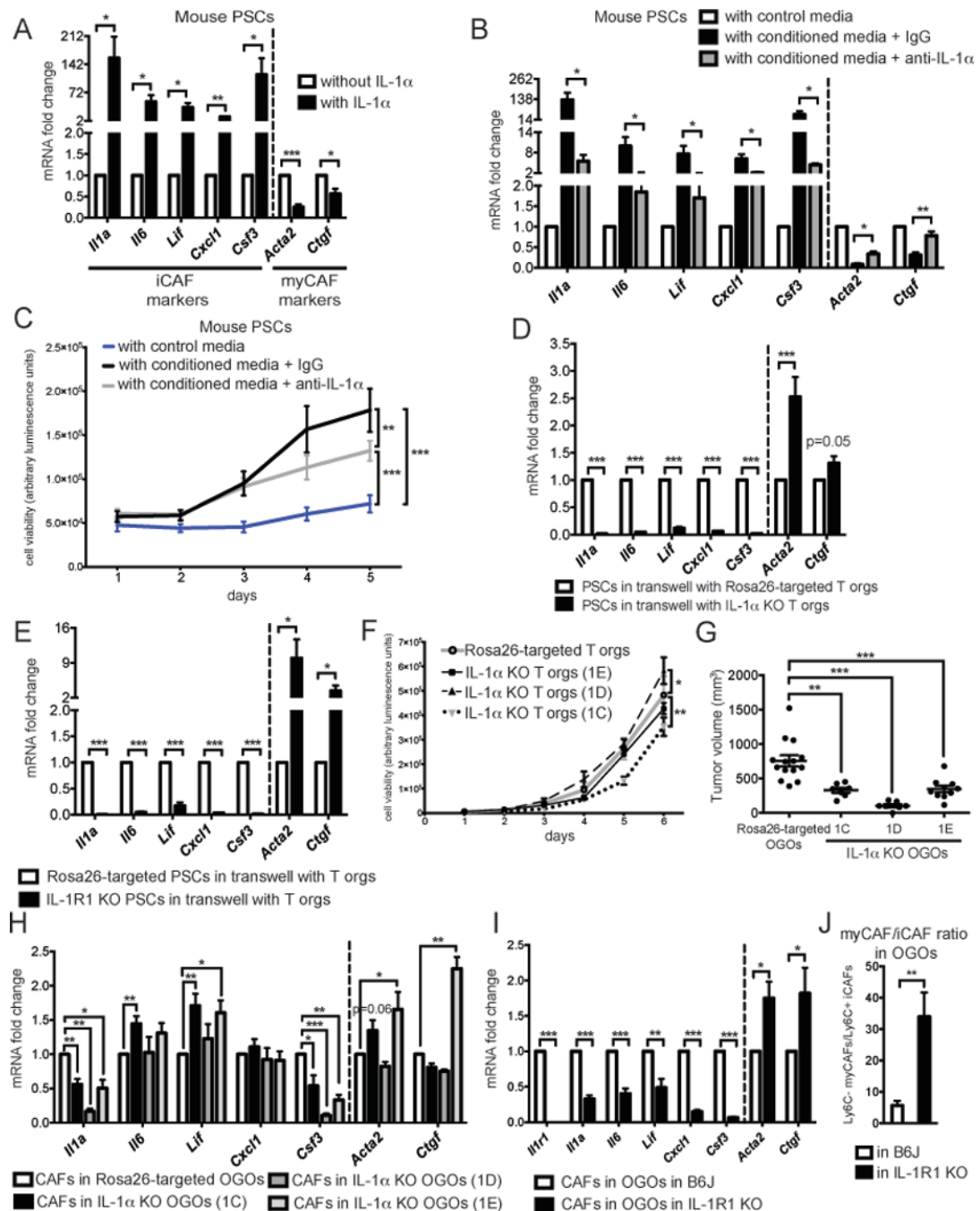


Figure 2: IL-1 signaling is the main pathway responsible for the induction of an inflammatory phenotype in CAFs.

A. qPCR analysis of iCAF (*Il1a*, *Il6*, *Lif*, *Cxcl1* and *Csf3*) and myCAF (*Acta2* and *Ctgf*) markers in PSCs cultured in Matrigel in control media in the presence or absence of 1 ng/mL mouse IL-1 α for 4 days. Results show mean \pm SEM of 2 biological replicates. * P <0.05, ** P <0.01, *** P <0.001, paired Student's t test. **B.** qPCR analysis of *Il1a*, *Il6*, *Lif*, *Cxcl1*, *Csf3*, *Acta2* and *Ctgf* in PSCs cultured in Matrigel with control media or tumor organoid-conditioned media in the presence of a neutralizing antibody targeting IL-1 α or an

IgG control for 4 days. Results show mean \pm SEM of 6 biological replicates. * $P < 0.05$, ** $P < 0.01$, paired Student's t test. **C.** Proliferation curves of PSCs cultured in Matrigel with control media or tumor organoid-conditioned media in the presence of a neutralizing antibody targeting IL-1 α or an IgG control. Results show mean \pm SEM of 3 biological replicates. ** $P < 0.01$, *** $P < 0.001$, unpaired Student's t test calculated for the last time point. **D.** qPCR analysis of *Il1a*, *Il6*, *Lif*, *Cxcl1*, *Csf3*, *Acta2* and *Ctgf* in PSCs cultured in Matrigel in transwell with Rosa26-targeted controls or IL-1 α knockout (KO) tumor organoids for 4 days. Results show mean \pm SEM of 9 and 11 biological replicates, respectively. *** $P < 0.001$, paired Student's t test. **E.** qPCR analysis of *Il1a*, *Il6*, *Lif*, *Cxcl1*, *Csf3*, *Acta2* and *Ctgf* in Rosa26-targeted controls and IL-1R1 knockout PSCs cultured in Matrigel in transwell with tumor organoids for 4 days. Results show mean \pm SEM of 7 biological replicates. * $P < 0.05$, *** $P < 0.001$, paired Student's t test. **F.** Proliferation curves of Rosa26-targeted controls and IL-1 α knockout tumor organoids. Results show mean \pm SD (standard deviation) of 5 technical replicates. * $P < 0.05$, ** $P < 0.01$, unpaired Student's t test calculated for the last time point. **G.** Tumor volume analysis based on ultrasound measurements of orthotopically grafted organoids (OGOs) following ~3 weeks from transplantation of Rosa26-targeted controls and IL-1 α knockout tumor organoids in nu/nu mice. Results show mean \pm SEM of 14 (control OGOs), 7 (1C or 1D OGOs) and 8 (1E OGOs) biological replicates. ** $P < 0.01$, *** $P < 0.001$, unpaired Student's t test. **H.** qPCR analysis of *Il1a*, *Il6*, *Lif*, *Cxcl1*, *Csf3*, *Acta2* and *Ctgf* in CAFs sorted from OGOs derived from transplantation of Rosa26-targeted controls and IL-1 α knockout tumor organoids in nu/nu mice. Results show mean \pm SEM of 4 (organoids), 12 (control OGOs) and 19 (IL-1 α knockout OGOs) biological replicates. Different symbols identify the 3 knockout lines. * $P < 0.05$, ** $P < 0.01$, *** $P < 0.001$, paired Student's t test. **I.** qPCR analysis of *Il1a*, *Il6*, *Lif*, *Cxcl1*, *Csf3*, *Acta2*, *Ctgf* and *Il1r1* in CAFs sorted from tumors derived by orthotopic transplantation of 3 tumor organoid lines in IL-1R1 knockout or C57BL/6J controls. Results show mean \pm SEM of 9 biological replicates. * $P < 0.05$, ** $P < 0.01$, *** $P < 0.001$, paired Student's t test. **J.** Quantification of Ly6C- myCAF/Ly6C+ iCAF ratio in tumors derived by orthotopic transplantation of 2 tumor organoid lines in B6J or IL-1R1 knockout hosts, as assessed by flow cytometry. Results show mean \pm SEM of 5 biological replicates. ** $P < 0.01$, unpaired Student's t test.

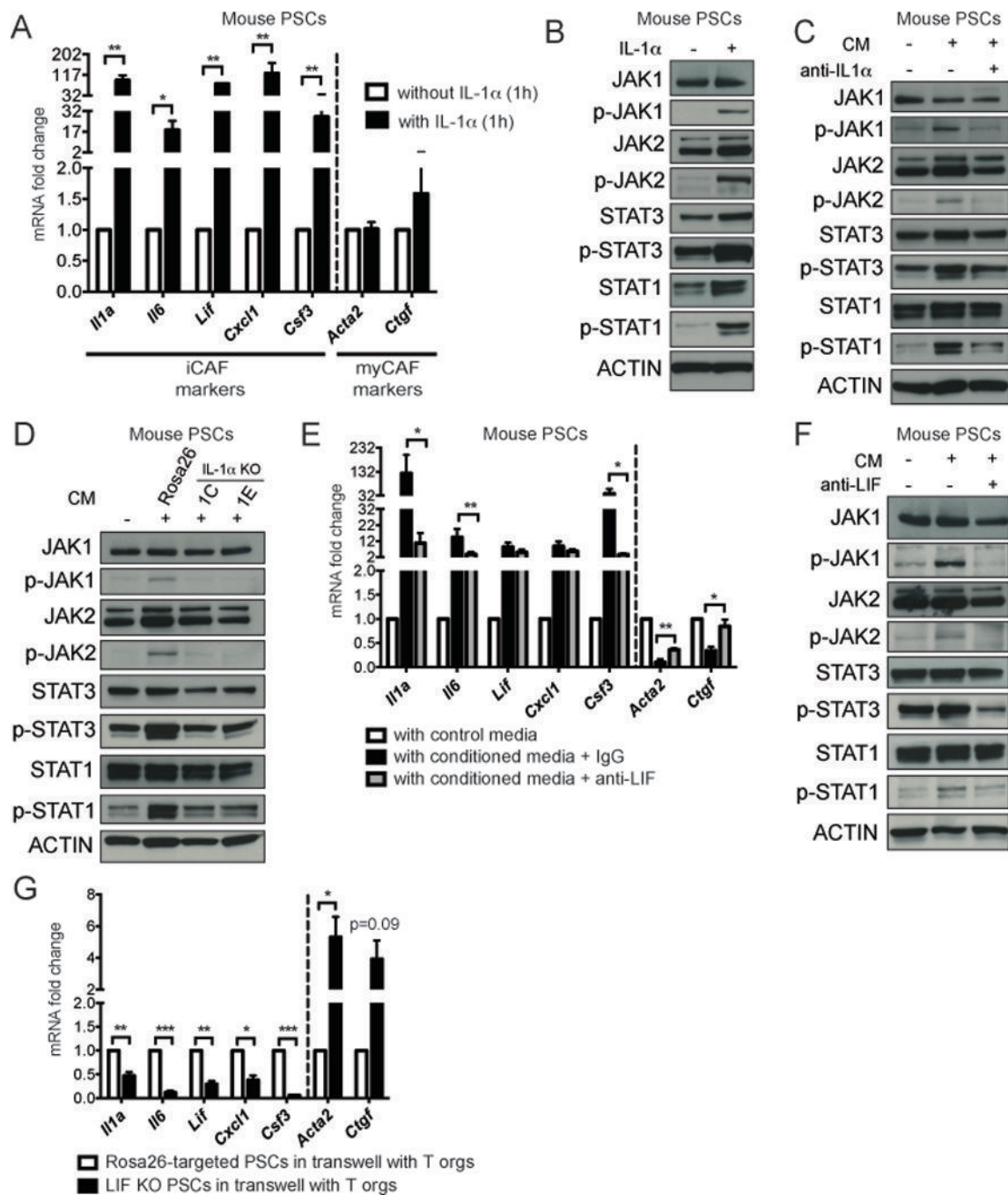


Figure 3: IL-1-mediated induction of autocrine LIF in PSCs activates JAK/STAT signaling and promotes iCAF formation.

A. qPCR analysis of iCAF (*Il1a*, *Il6*, *Lif*, *Cxcl1* and *Csf3*) and myCAF (*Acta2* and *Ctgf*) markers in PSCs cultured in Matrigel in control media in the presence or absence of 1 ng/mL mouse IL-1 α for 1 h. Results show mean \pm SEM of 2 biological replicates. *P<0.05, **P<0.01, paired Student's *t* test. **B.** Western blot analysis of p-JAK1, JAK1, p-JAK2, JAK2, p-STAT1, STAT1, p-STAT3 and STAT3 in PSCs cultured in Matrigel with control media in the presence or absence of 1 ng/mL mouse IL-1 α for 4 days. Loading control, ACTIN. **C.**

Western blot analysis of p-JAK1, JAK1, p-JAK2, JAK2, p-STAT1, STAT1, p-STAT3 and STAT3 in PSCs cultured in Matrigel with control media or tumor organoid-conditioned media (CM) in the presence of a neutralizing antibody targeting IL-1 α or an IgG control for 4 days. Loading control, ACTIN. **D.** Western blot analysis of p-JAK1, JAK1, p-JAK2, JAK2, p-STAT1, STAT1, p-STAT3 and STAT3 in PSCs cultured in Matrigel with control media or tumor organoid-conditioned media (CM) from Rosa26-targeted controls or IL-1 α knockout tumor organoids for 4 days. Loading control, ACTIN. **E.** qPCR analysis of *Il1a*, *Il6*, *Lif*, *Cxcl1*, *Csf3*, *Acta2* and *Ctgf* in PSCs cultured in Matrigel with control media or tumor organoid-conditioned media in the presence of a neutralizing antibody targeting LIF or an IgG control for 4 days. Results show mean \pm SEM of 6 biological replicates. *P<0.05, **P<0.01, paired Student's *t* test. **F.** Western blot analysis of p-JAK1, JAK1, p-JAK2, JAK2, p-STAT1, STAT1, p-STAT3 and STAT3 in PSCs cultured in Matrigel with control media or tumor organoid-conditioned media (CM) in the presence of a neutralizing antibody targeting LIF or an IgG control for 4 days. Loading control, ACTIN. **G.** qPCR analysis of *Il1a*, *Il6*, *Lif*, *Cxcl1*, *Csf3*, *Acta2* and *Ctgf* in LIF knockout PSCs compared to Rosa26-targeted controls cultured in Matrigel in transwell with tumor organoids for 4 days. Results show mean \pm SEM of 4 biological replicates. *P<0.05, **P<0.01, ***P<0.001, paired Student's *t* test.

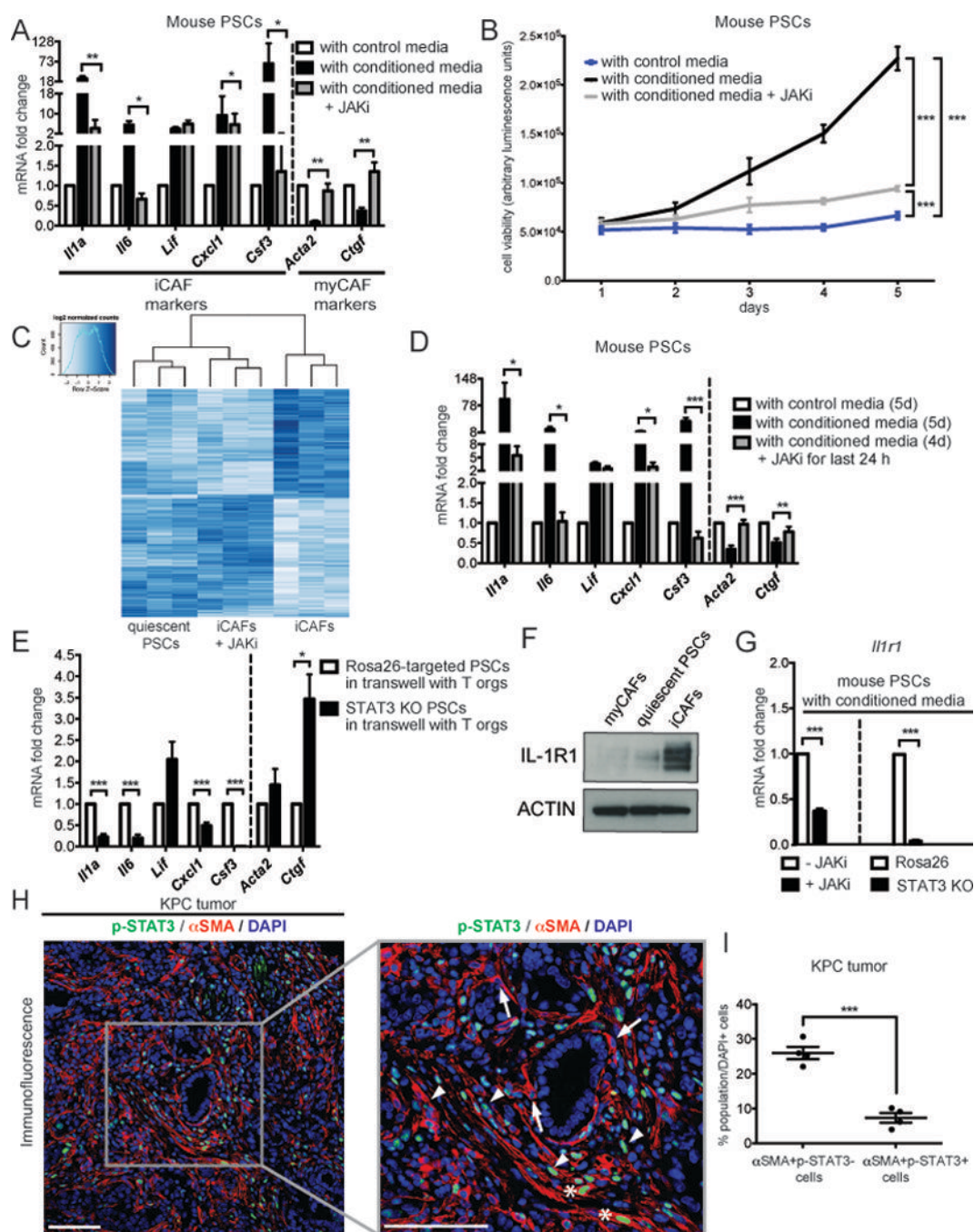


Figure 4: JAK/STAT signaling mediates the induction of the iCAF phenotype.

A. qPCR analysis of iCAF (*Il1a*, *Il6*, *Lif*, *Cxcl1* and *Csf3*) and myCAF (*Acta2* and *Ctgf*) markers in PSCs cultured in Matrigel with control media or tumor organoid-conditioned media in the presence or absence of 500 nM JAK inhibitor (JAKi) AZD1480 for 4 days. Results show mean \pm SEM of 5 biological replicates. * $P < 0.05$, ** $P < 0.01$, paired Student's *t* test. **B.** Proliferation curves of PSCs cultured in Matrigel with control media or tumor organoid-conditioned media in the presence or absence of 500 nM JAKi. Results show mean \pm SEM of 3 biological replicates. *** $P < 0.001$, unpaired Student's *t* test calculated for the

last time point. **C.** RNA-sequencing analysis of quiescent PSCs (n=3), iCAFs (n=3) and iCAFs treated with 500 nM JAKi for 4 days (n=3). Color scheme represents Z-score distribution. **D.** qPCR analysis of *Il1a*, *Il6*, *Lif*, *Cxcl1*, *Csf3*, *Acta2* and *Ctgf* in PSCs cultured in Matrigel with control media or tumor organoid-conditioned media in the presence or absence of 500 nM JAKi for the last 24 h following 4 days in culture with conditioned media. Results show mean \pm SEM of 5 biological replicates. *P<0.05, **P<0.01, ***P<0.001, paired Student's *t* test. **E.** qPCR analysis of *Il1a*, *Il6*, *Lif*, *Cxcl1*, *Csf3*, *Acta2* and *Ctgf* in Rosa26-targeted controls and STAT3 knockout PSCs cultured in Matrigel in transwell with tumor organoids for 4 days. Results show mean \pm SEM of 5 biological replicates. *P<0.05, ***P<0.001, paired Student's *t* test. **F.** Western blot analysis of IL-1R1 in myCAFs, quiescent PSCs and iCAFs. Loading control, ACTIN. **G.** qPCR analysis of *Il1r1* in PSCs cultured in Matrigel with tumor organoid-conditioned media in the presence or absence of 500 nM JAKi (left) and in STAT3 knockout PSCs compared to controls (right). Results show mean \pm SEM of 4 and 5 biological replicates, respectively. ***P<0.001, paired Student's *t* test. **H.** Representative immunofluorescence co-stains of p-STAT3 (green) and α SMA (red) in KPC tumor sections (n=4). Counterstain, DAPI (blue). Arrows indicate examples of α SMA+ p-STAT3- myCAFs, arrow-heads indicate examples of α SMA- p-STAT3+ cells, asterisks indicate examples of α SMA+ p-STAT3+ cells. Scale bars, 100 μ m. **I.** Quantification of α SMA+ p-STAT3- cells and α SMA+ p-STAT3+ cells in KPC tumor sections. Results show mean \pm SEM of 4 biological replicates. ***P<0.001, unpaired Student's *t* test.

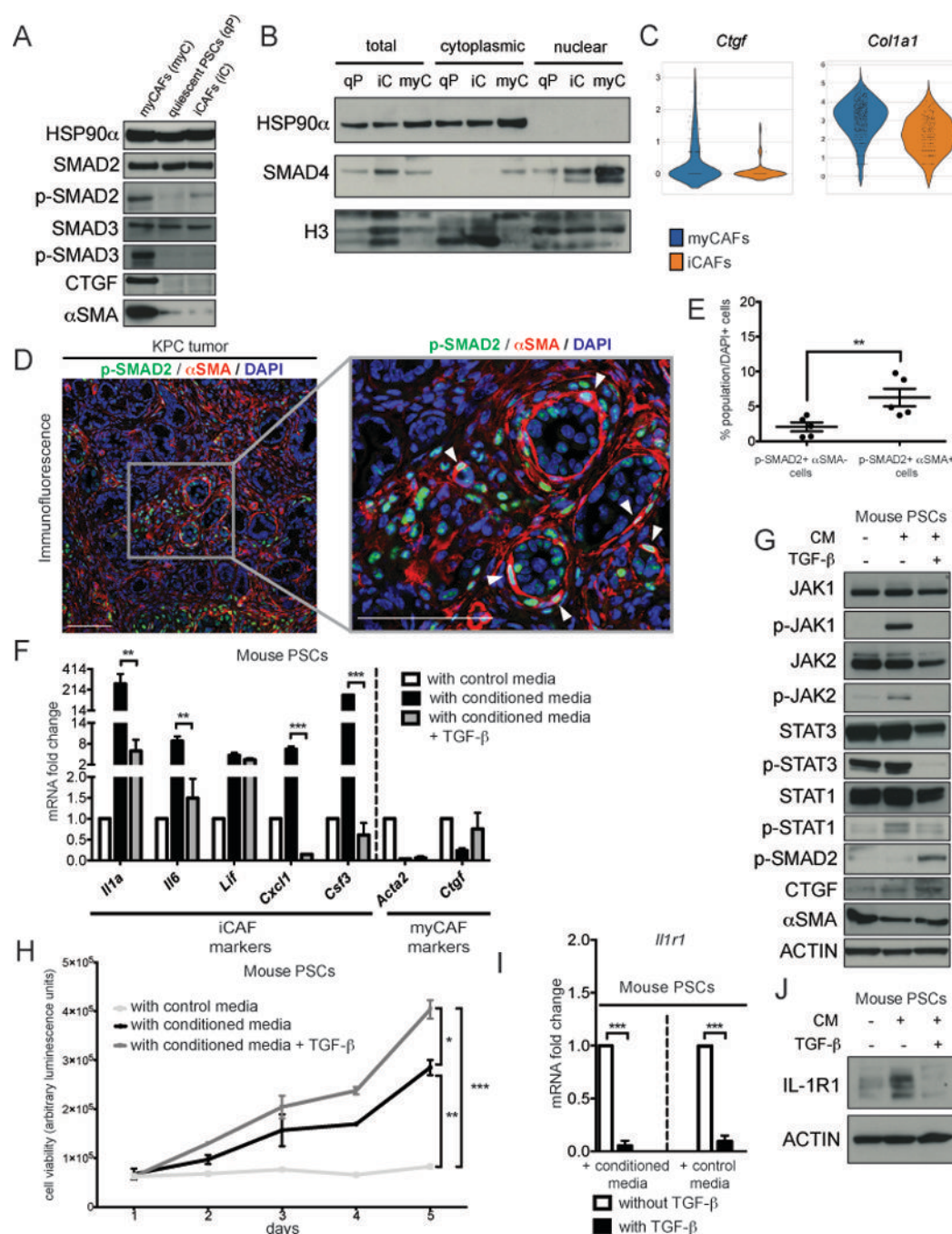


Figure 5: TGF- β signaling antagonizes IL-1-induced JAK/STAT signaling and inhibits the iCAF phenotype.

A. Western blot analysis of SMAD2, p-SMAD2, SMAD3, p-SMAD3, CTGF and α SMA in myCAFs (myC), quiescent PSCs (qP) and iCAFs (iC). Loading control, HSP90 α . **B.** Western blot analysis of the TGF- β signaling effector SMAD4 following nuclear fractionation of quiescent PSCs (qP), iCAFs (iC) and myCAFs (myC). Loading controls, HSP90 α (cytoplasmic fractions) and H3 (nuclear fractions). The same amount of protein lysate was loaded in each lane. **C.** Violin plots showing single cell RNA-sequencing analysis

of *Ctgf* and *Col1a1* of a representative KPC tumor (n=2) in myCAFs (blue) and iCAFs (orange). **D.** Representative immunofluorescence co-stains of p-SMAD2 (green) and α SMA (red) in KPC tumor sections (n=5). Counterstain, DAPI (blue). Arrow-heads indicate examples of α SMA+ p-SMAD2+ cells. Scale bars, 100 μ m. **E.** Quantification of p-SMAD2+ α SMA- cells and p-SMAD2+ α SMA+ cells in KPC tumor sections. Results show mean \pm SEM of 5 biological replicates. **P<0.01, paired Student's *t* test. **F.** qPCR analysis of iCAF (*Il1a*, *Il6*, *Lif*, *Cxcl1* and *Csf3*) and myCAF (*Acta2* and *Ctgf*) markers in PSCs cultured in Matrigel with control media or tumor organoid-conditioned media in the presence or absence of 20 ng/mL mouse TGF- β for 4 days. Results show mean \pm SEM of 6 biological replicates. **P<0.01, ***P<0.001, paired Student's *t* test. **G.** Western blot analysis of p-JAK1, JAK1, p-JAK2, JAK2, p-STAT1, STAT1, p-STAT3, STAT3, p-SMAD2, CTGF and α SMA in PSCs cultured in Matrigel with control media or tumor organoid-conditioned media (CM) in the presence or absence of 20 ng/mL mouse TGF- β for 4 days. Loading control, ACTIN. **H.** Proliferation curves of PSCs cultured in Matrigel with control media or tumor organoid-conditioned media in the presence or absence of 20 ng/mL mouse TGF- β . Results show mean \pm SD of 5 technical replicates. *P<0.05, **P<0.01, ***P<0.001, unpaired Student's *t* test calculated for the last time point. **I.** qPCR analysis of *Il1r1* in PSCs cultured in Matrigel with control media or tumor organoid-conditioned media in the presence or absence of 20 ng/mL mouse TGF- β for 4 days. ***P<0.001, paired Student's *t* test. **J.** Western blot analysis of IL-1R1 in PSCs cultured in Matrigel with control media or tumor organoid-conditioned media in the presence or absence of 20 ng/mL mouse TGF- β for 4 days. Loading control, ACTIN.

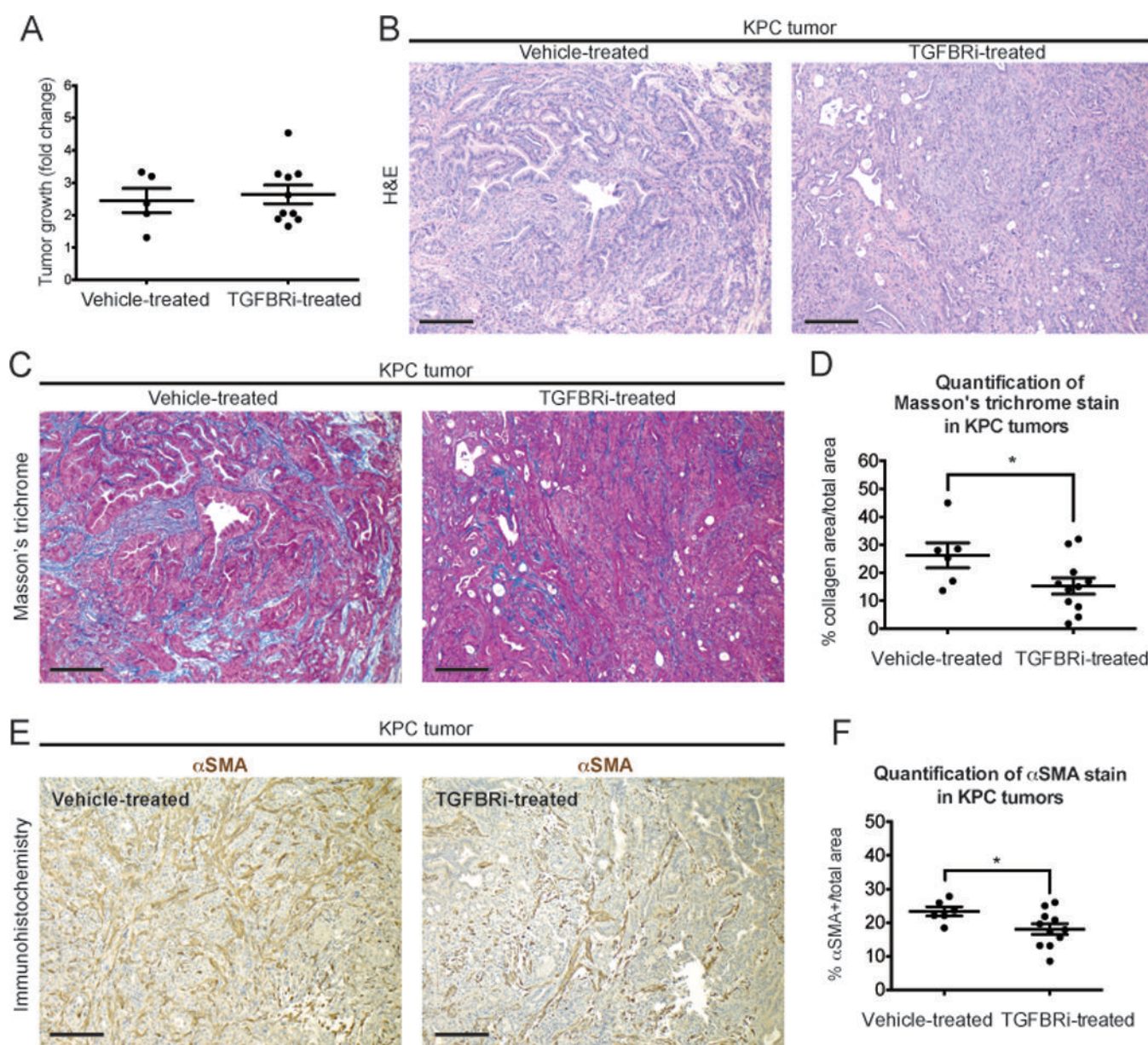


Figure 6: Inhibition of TGF- β signaling targets myofibroblasts *in vivo*.

A. Tumor volume analysis based on ultrasound measurements of vehicle- and TGFBRI- treated KPC tumors. Results show mean \pm SEM of 5 and 10 tumors, respectively. No statistical difference was found, as calculated by unpaired Student's *t* test.

B. Representative Hematoxylin and Eosin (H&E) stain of vehicle- and TGFBRI- treated KPC tumor sections (n= 6 and 11, respectively). Scale bar, 200 μ m. **C.** Representative Masson's trichrome stain of 10-day vehicle- and TGFBRI- treated KPC tumor sections (n= 6 and 11, respectively). Scale bar, 200 μ m. **D.** Quantification of Masson's trichrome stain in vehicle- and TGFBRI- treated KPC tumors. Results show mean \pm SEM of 6 biological replicates. *P<0.05, unpaired Student's *t* test. **E.** Representative immunohistochemistry of α SMA stain of vehicle- and TGFBRI- treated KPC tumor sections (n= 6 and 11, respectively). Scale bar, 200 μ m. **F.** Quantification of α SMA stain in vehicle- and TGFBRI-

treated KPC tumors. Results show mean \pm SEM of 6 and 11 biological replicates, respectively. * $P < 0.05$, unpaired Student's t test.

Author Manuscript

Author Manuscript

Author Manuscript

Author Manuscript

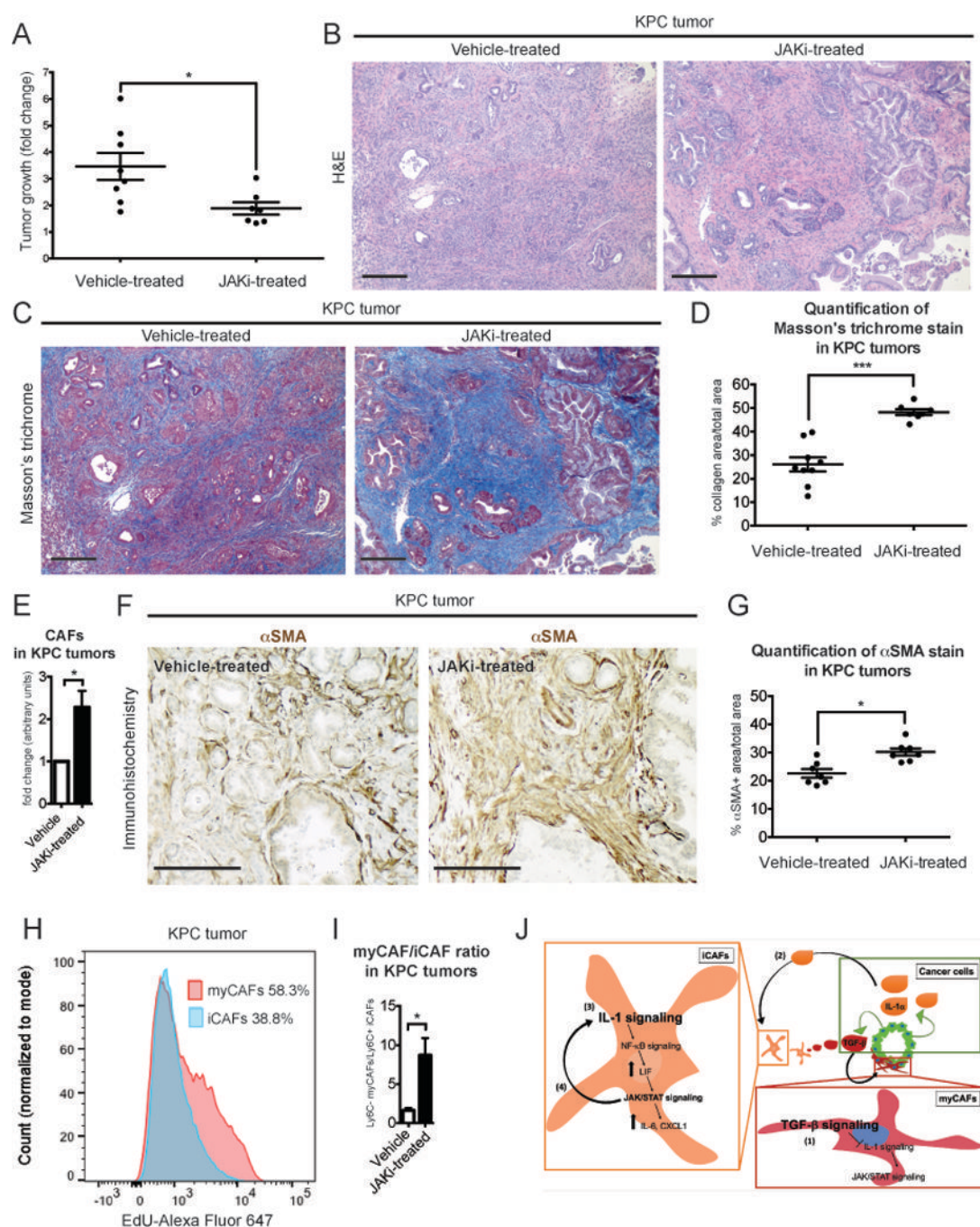


Figure 7: JAK inhibition shifts iCAFs to a myofibroblastic phenotype *in vivo*.

A. Tumor volume analysis based on ultrasound measurements of vehicle- and JAK inhibitor (JAKi)- treated KPC tumors. Results show mean \pm SEM of 8 and 7 tumors, respectively. *P < 0.05, unpaired Student's *t* test. **B.** Representative Hematoxylin and Eosin (H&E) stain of vehicle- and JAKi- treated KPC tumor sections (n=9 and 7, respectively). Scale bar, 200 μ m. **C.** Representative Masson's trichrome stain of vehicle- and JAKi- treated KPC tumor sections (n= 9 and 7, respectively). Scale bar, 200 μ m. **D.** Quantification of Masson's trichrome stain in vehicle- and JAKi- treated KPC tumors. Results show mean \pm SEM of 9

and 7 biological replicates, respectively. *** $P < 0.001$, unpaired Student's t test. **E.** Quantification of CAFs in vehicle- and JAKi- treated KPC tumors, as assessed by flow cytometry. Results show mean \pm SEM of 4 biological replicates. * $P < 0.05$, unpaired Student's t test. **F.** Representative immunohistochemistry of α SMA stain of vehicle- and JAKi- treated KPC tumor sections ($n=7$). Scale bar, 200 μ m. **G.** Quantification of α SMA stain in vehicle- and JAKi- treated KPC tumors. Results show mean \pm SEM of 7 biological replicates. * $P < 0.05$, unpaired Student's t test. **H.** Representative flow cytometric analysis of iCAFs and myCAFs in EdU-treated KPC tumors ($n=2$). The values shown represent the EdU + cells in each CAF population. **I.** Quantification of Ly6C- myCAF/Ly6C+ iCAF ratio in vehicle- and JAKi- treated KPC tumors, as assessed by flow cytometry. Results show mean \pm SEM of 3 biological replicates. * $P < 0.05$, unpaired Student's t test. **J.** Model explaining the pathway antagonism that determines iCAF and myCAF formation in PDAC. (1) Tumor-secreted TGF- β activates TGF- β signaling in adjacent myCAFs, preventing induction of the iCAF phenotype by suppressing IL-1R1 expression. (2) Conversely, tumor-secreted IL-1 activates IL-1 signaling in CAFs that are located farther away from tumor glands. (3) In these CAFs, IL-1 signaling induces a cytokine cascade that leads to JAK/STAT signaling activation through NF- κ B signaling and autocrine LIF. (4) The activated JAK/STAT pathway establishes a positive feedback loop by upregulating IL-1R1 expression.